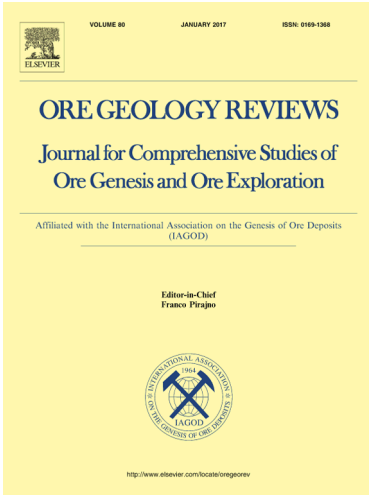

Oxide chemistry and fluid inclusion constraints on the formation of itabirite-hosted iron ore deposits at the eastern border of the Southern Espinhaço Range, Brazil

Sylvio D. Gomes, Sarah Berger, Rosaline C. Figueiredo e Silva, Steffen G. Hagemann, Carlos A. Rosière, David A. Banks, Lydia M. Lobato, Ana-Sophie Hensler

PII: S0169-1368(17)30951-4
DOI: https://doi.org/10.1016/j.oregeorev.2018.03.025
Reference: OREGEO 2541

To appear in: *Ore Geology Reviews*

Received Date: 8 December 2017
Revised Date: 22 March 2018
Accepted Date: 27 March 2018

Please cite this article as: S.D. Gomes, S. Berger, R.C. Figueiredo e Silva, S.G. Hagemann, C.A. Rosière, D.A. Banks, L.M. Lobato, A-S. Hensler, Oxide chemistry and fluid inclusion constraints on the formation of itabirite-hosted iron ore deposits at the eastern border of the Southern Espinhaço Range, Brazil, *Ore Geology Reviews* (2018), doi: https://doi.org/10.1016/j.oregeorev.2018.03.025

Oxide chemistry and fluid inclusion constraints on the formation of itabirite-hosted iron ore deposits at the eastern border of the Southern Espinhaço Range, Brazil

Sylvio D. Gomes[a,*], Sarah Berger[b], Rosaline C. Figueiredo e Silva[a], Steffen G. Hagemann[b], Carlos A. Rosière[a], David A. Banks[c], Lydia M. Lobato[a], Ana-Sophie Hensler[d]

[a] Universidade Federal de Minas Gerais, CPMTC, Instituto de Geociências, Av.Presidente Antônio Carlos, 6627, Pampulha, Belo Horizonte, MG, Brazil

[b] University of Western Australia, Centre for Exploration Targeting, Nedlands-WA 6009, Australia

[c] School of Earth and Environment, University of Leeds, Woodhouse Lane, Leeds LS2 9JT, United Kingdom

[d] Institute of Mineral Resources Engineering, RWTH Aachen University, Aachen, Germany

[*] Corresponding author

E-mail address: sylvio.gomes@gmail.com

Abstract

The Piçarrão and Liberdade deposits contain high-grade iron orebodies (> 65% Fe) hosted in the Guanhães Group itabirite, that are associated with pegmatite veins and bodies. Fluid inclusion studies in quartz veins associated with the high-grade orebodies show that medium to high salinities (25-28 wt. % NaCl eq.) and temperatures (275-375 ^{o}C) fluids are associated with the silica leaching that led to the iron enrichment. Mineral chemistry studies by LA-ICP-MS in the iron oxides demonstrate that metasomatic processes were responsible for the mineralogical transformations of magnetite to hematite and for subsequent hematite recrystallization. These processes are related to the iron upgrade in the itabirite and the formation of high-grade orebodies. The oxidation of the magnetite to martite is associated with an enrichment in P and As, and depletion in Mg, Ti and Co; as observed in martite crystals compared to their matching kenomagnetite rims. On the other hand Ti and Mo are enriched in hematite crystals that recrystallized from martite. In this case Ti behaved as an immobile element, and its enrichment is accompanied by the depletion of most of the trace elements. A second stage of magnetite formation precipitated with quartz in discordant veins and is oxidized to martite-II. These quartz-martite-II veins contain low salinity and temperature fluid inclusions that record an episode of meteoric fluid influx. The results of the LA-ICP-MS analyses on the fluid inclusions from pegmatite and quartz veins associated with the high-grade iron bodies indicate the contribution of anatectic fluids in the evolution of the metasomatic events.

Keywords

Fluid inclusions
LA-ICP-MS
Iron ore

1. Introduction

High-grade (> 65 wt. % Fe) iron ore deposits are the most important Fe metal source (production and reserve) worldwide. These deposits are commonly hosted in banded iron formations (BIF), which are defined as chemical sedimentary rocks composed of chert layers (bands) and containing at least 15 wt. % of iron (Beukes and Gutzmer, 2008; Klein, 2005).

The iron formation-hosted iron ore system is defined as ore located and derived from BIF. The transformation of iron formation to high-grade iron ore is controlled by: (1) structural permeability; (2) hypogene alteration caused by ascending deep hydrothermal fluids (largely magmatic or basinal brines), and descending ancient meteoric water; and (3) supergene enrichment via weathering processes (Hagemann et al., 2016). The hypogene iron enrichment is characterized by silica and carbonate leaching, and changes in the iron oxides mineralogy and textures.

The name itabirite is used to describe metamorphosed and deformed banded iron formations (Dorr, 1969). There are two main itabirite-hosted iron ore provinces in southeastern Brazil: Quadrilátero Ferrífero (QF) and the eastern border of the southern Espinhaço Range (SER). Both provinces are located at the southern portion of the São Francisco Craton (Almeida, 1977; Almeida et al., 2000) in Minas Gerais state (Fig. 1).

The geology of QF is composed of three main units: granite–gneiss terranes; the Rio das Velhas greenstone belt, and Proterozoic metasedimentary sequences (Dorr, 1969), with the latter encompassing the Minas Supergroup, Itacolomi Group and Espinhaço Supergroup.

The Minas Supergroup is a metasedimentary unit containing a thick Lake Superior-type (Klein, 2005) sequence of iron formation which was metamorphosed during the Paleoproterozoic Transamazonian tectono-thermal orogenic event (Machado et al., 1992; Alkmim and Marshak, 1998). During this event, hydrothermal hypogene alteration, second order flexural and flexural-slip folds and reverse shear zones controlled the distribution of economically important itabirite-hosted high-grade iron ore deposits, typically >64 wt. % Fe (Rosière et al., 2008).

In the SER there are itabirite-bearing metasedimentary sequences that were deposited in a rift and rift-sag epicontinental environment; and that can be correlated with the Espinhaço Supergroup, Guanhães Group and with the Costa Sena Group (Grossi-Sad et al., 1997, Braga et al., 2015, Rolim et al., 2016). These sequences occur as thrust slices, associated with granitic-gneiss rocks of the Guanhães Complex, developed during the tectono-thermal Neoproterozoic-Early Paleozoic Brasiliano/Pan-African orogenic event (e.g., Alkmim et al., 2006). This area is located at the western portion of the Eastern Brazilian Pegmatite Province (Fig. 1), constituting the most important Brazilian gemological province (Correia Neves et al., 1986; Morteani et al., 2000). Pegmatites within SER have an anatectic origin and intruded during the Brasiliano orogen (Bilal et al., 1995; Marciano et al.,1993). The Ponte da Raiz beryl deposit is located 5 km NE of the town of Santa Maria de Itabira (Fig. 2) and is hosted in tabular shaped pegmatite intrusive in the gneiss of

the Guanhães Complex.

Due to the increasing global demand for iron in the last 15 years, an intensive exploration program has been developed in the SER providing a large amount of new data through diamond drilling, detailed geological mapping and geophysical surveys. In 2014, Anglo American started production at the first iron mine in the Serra da Serpentina range (Anglo American, 2014).

The Piçarrão-Liberdade iron deposit (PLD) is located approximately 20 km NE of the town of Itabira and represents a resource of 5.31 Mt of iron ore at an average grade of 43.3 wt. % Fe (Centaurus, 2008). The PLD was mined by VALE from 1976 to the late 1980's, and contains high-grade, tabular-shaped iron orebodies, with 20 m thick layers, striking to the NE for 5 km. Pegmatites and quartz veins are commonly associated with the high-grade orebodies in this deposit. The Morro Escuro ridge is located at the northern limit of the town of Santa Maria de Itabira, and comprises a metasedimentary itabirite-bearing sequence forming a NE-striking thrust slice in the Guanhães Complex rocks (Carvalho et al., 2014; Braga et al., 2015). The itabirite layer is exposed along the ridge for about 20 km and has a 15 m average thickness. Both PLD and Morro Escuro ridge are located at the southern portion of the eastern border of the Espinhaço Range (Fig. 1).

Geological processes responsible for the hypogene upgrade of itabirite to high-grade iron deposits in the Espinhaço Range (Oliveira et al., 2017; Rolim, 2016) is controversial and the nature of the hydrothermal fluids involved is unknown. This study addresses this controversy by using detailed mineralogy and paragenetic studies, together with whole rock geochemistry, mineral chemistry and fluid inclusions techniques to investigate the composition of iron oxides and fluid inclusions from quartz veins and pegmatites located at the Piçarrão-Liberdade iron deposit and Morro Escuro ridge. Results from these analyses are used to propose a hydrothermal model that constrains mineralizing processes and fluid sources, which led to the enrichment of itabirite to high-grade iron ore. In addition, itabirite from the more northern Guanhães and Dores de Guanhães areas (Fig. 1) were studied in terms of their whole rock geochemistry and mineral chemistry in order to evaluate the similarities of the depositional and metamorphic/hydrothermal process over a wide geographical range within the Guanhães Group.

2. Geological setting of the southern Espinhaço Range

The southern Espinhaço Range is located at the external, western zone of the Neoproterozoic Araçuaí fold belt (Almeida 1977; Alkimim et al., 2006; Pedrosa Soares et al., 2001, 2007). This is a NS-trending and west-verging system of faults and folds on the southeastern edge of the São Francisco Craton that incorporates Archean-Paleoproterozoic basement and supracrustal rocks of the Espinhaço Supergroup (Fig. 1). In the external zone, the Archean-Paleoproterozoic basement is composed of the Guanhães Complex and the Borrachudos Suite (Alkmim et al., 2006; Noce et

al., 2007).

The São Francisco Craton is defined as a stable part of the South American platform. As a single continental block following the Paleoproterozoic it was not involved in the Brasiliano/Pan-African orogen during the Neoproterozoic, between 600 and 480 Ma (Cordani et al., 2010). The Craton has a long history of intracratonic and passive margin basin filling, magmatism and orogenic build-up (Almeida, 1977; Chemale et al., 1998; Silveira et al., 2013), and its basement records an important tectono-magmatic evolution during the Paleoproterozoic - Transamazonian/Eburnean orogen (2.2 to 2.0 Ga; Barbosa and Sabaté, 2004; Noce et al., 2007).

The Espinhaço Basin forms part of a complex rift system, extending approximately 1090 km north-south (Fig. 1), that developed as an intracontinental rift-sag basin on the São Francisco Craton during the Paleo – Mesoproterozoic (Martins-Neto, 2000; Chemale et al., 2012; Guadagnin et al., 2015). This extensional event was accompanied by the emplacement of anorogenic granites of the Borrachudos Suite within granite-gneiss-migmatitic rocks of the Archean basement rocks grouped in the Guanhães Complex (Dussin and Dussin, 1995), and by the deposition of the Espinhaço Supergroup. The Espinhaço Supergroup comprises a more than 5000 m thick sequence of metasandstone, metaconglomerate, metapelite, bimodal volcanic and subordinate carbonate rocks (Pflug, 1965; Grossi-Sad et al., 1997; Uhlein et al., 1998; Martins-Neto, 2000). The U-Pb detrital zircon dating established two rift stages for the Espinhaço Supergroup deposition (Chemale Jr. et al., 2012): a rift-sag sequence accumulated between 1192 and 906 Ma (Stenian-Upper Espinhaço); and a rift sequence accumulated between 1.68 and 1.80 Ga (Statherian-Lower Espinhaço).

During the Neoproterozoic, between 1000 and 850 Ma, a second episode of rifting occurred in the region with the development of a narrow ocean basin (Pedrosa Soares et al., 2001). The sedimentary fill of this Neoproterozoic basin comprises the Macaúbas Group (Uhlein et al., 1998; Martins-Neto and Hercos, 2002; Pedrosa-Soares et al., 2000).

During the Brasiliano orogen, the assembly of West Gondwana resulted in the closure of the rift basins (Espinhaço and Macaúbas), and the development of the Araçuaí fold belt (Fig. 1). At the contact between the São Francisco Craton and the Araçuaí fold belt the basin rocks are deformed and portions of the reworked Archean and Paleoproterozoic basement are exposed (Dussin and Dussin, 1995; Uhlein et al., 1998; Pedrosa-Soares et al., 2001; Alkmim et al., 2006; Noce et al., 2007). The tectonic evolution of the Araçuaí belt is well documented with granitic magmatism in the 630 to 480 Ma time range: pre-collisional (G1 suite – 630 to 580 Ma); syn-collisional (G2 and G3 suites – 585 to 530 Ma); and post-collisional (539 to 480 Ma G4 and G5 suites). The post-collisional granites have been interpreted to be related to the gravitational collapse of the orogeny (Campos et al., 2016; Melo et al., 2017).

The Guanhães Complex is composed of tonalite-trondhjemite-granodiorite (TTG) gneisses, migmatites and granites. Geochronological studies (SHRIMP U/Pb; Silva et al., 2002) on the TTG gneissic complex yield 2.7-2.8 Ga magmatic crystallization age, and 519-527 Ma metamorphic

age. From $\text{TM}^{18}O$ data on quartz/garnet/biotite, Muller et al. (1986a) deduced a temperature between 462 and 612 °C for the Brasiliano regional metamorphism at the Guanhães Complex. From the $\text{TM}^{18}O$ data on the quartz/magnetite mineral pair from the itabirite of the Piçarrão mine, it was deduced a higher metamorphic temperature from 606 to 814 °C Muller et al. (1986b).

The Guanhães Complex is associated with discontinuous units of metasedimentary rocks of the Guanhães Group (Grossi-Sad et al., 1990b; 1997; Noce et al., 2007). This group of rocks were metamorphosed to amphibolite facies. Itabirite layers with a thickness from 15 to 60 m have variable contents of amphibole (5-20%), carbonate and chlorite (1-10%). According to Barrote (2016) the basal quartzite is 50 m thick, containing intercalations of sericitic, arkosic and iron-rich quartzites associated with layers of gneiss and schist. The upper unit has coarse-grained quartzite interlayered with centimetric to metric bands of garnet-rich amphibolite. Detrital zircon geochronological analyses from quartzite of the Guanhães Group established deposition no older than Rhyacian (maximum age of 2080 Ma; Barrote, 2016).

Several granitic plutons of the Borrachudos Suite occur in the Guanhães Complex (Grossi-Sad et al., 1990a; Dussin and Dussin, 1995). This denomination was first used by Dorr and Barbosa (1963) to describe a granitic pluton NW of Itabira. Geochronological and geochemical data of the Borrachudos Suite indicate magma genesis at 1.7 Ga in the anorogenic context of crustal extension and melting of lower crustal rocks related to the rift event that led to the deposition of the Espinhaço Supergroup (Dossin et al., 1993; Fernandes et al., 1994; Dussin, 1994; Dussin et al., 2000; Fernandes, 2001; Silva et al., 2002).

The Guanhães Complex and the Borrachudos Suite host a wide number of pegmatite bodies that are 1-10 m thick, generally tabular-discordant in shape, and that host beryl deposits and other types of gems (eg. alexandrite, emerald); these deposits are grouped in the Santa Maria de Itabira (or Nova Era – Itabira – Ferros) pegmatite district (Pedrosa Soares et al., 2011). This district is part of the Brazilian eastern pegmatite province (Marciano, 1995; Morteani et al., 2000; Preinfalk et al., 2002) and have an anatectic origin during the Brasiliano tectono-thermal event according to the dating of igneous monazite (531 Ma; Bilal et al., 1995); muscovite (519 Ma; Marciano et al., 1993) and titanite (576 Ma; Jordt-Evangelista et al., 2016). In this portion of the pegmatite province, pegmatites were produced by partial melting of the basement. In the case of the Ponte da Raiz deposit the beryl crystals occur in the intermediate zone associated mainly with quartz and K-feldspar. This pegmatite-forming event is more or less coeval with the intrusion of the post-tectonic S-type granites, emplaced mainly in the eastern portion of the Araçuaí belt during the late stages of the Brasiliano orogen (Pedrosa-Soares et al., 2011).

The most important itabirite bearing metasedimentary sequences in the SER crops out at the Serra da Serpentina Range (Almeida-Abreu and Renger 2002). Based on detrital zircon dating and structural mapping, Rolim et al. (2016) established two itabirite-bearing metasedimentary sequences at this range: São José and Serra da Serpentina Groups. The São Jose Group was

deposited on a tectonically active continental rift basin with a maximum depositional age of 1666 ± 32 Ma (Statherian); it is correlated with the Lower Espinhaço Supergroup and the early stages of the opening of the Espinhaço basin. The Serra da Serpentina Group was deposited on a sag basin with little tectonic activity with a maximum depositional age of 1990 ± 16 Ma (Orosirian) and is correlated with the pre-Espinhaço Costa Sena Group. This Orosirian sequence is separated from the overlying São José Group by an erosional unconformity. The itabirite layer thickness varies from 20 to 40 m in the São José Group, and from 15 to 350 m in the Serra da Serpentina Group. Barrote (2016) established the correlation between the Guanhães and Serra da Serpentina Groups based on the similar age distributions of detritic zircons.

3. Sampling and analytical methods

3.1. Whole rock geochemistry

Thirty representative samples (itabirite and ores) from all localities were analyzed for major oxide, trace element (TE) and rare earth elements (REE) whole rock geochemistry at the Activation Laboratories in Ontario, Canada. Martite-II crystals were extract from quatrz-martite veins (Vp2) from the PLD deposit and analyzed separately.

Carbon and sulfur were analyzed by IR absorption spectroscopy and FeO through titration using a cold acid digestion of ammonium metavanadate and hydrofluoric acid. Trace elements and REE were analyzed by both four acid digestion followed by ICP-MS and lithium borate fusion and aqua regia digestion followed by ICP-MS. Loss on ignition (LOI) at 1000° C was measured gravimetrically and gives an indication of the total weight of volatiles in each sample. Analytical accuracy was tested with an externally submitted powder of the FeR-3 BIF international standard (Bau and Alexander, 2009), with an achieved accuracy of ±1.25 %SD. Precision was measured by the analysis of identical duplicate samples with an error of ±3 %RSD.

3.2. Iron oxide LA-ICP-MS studies

Eighteen samples were selected for in-situ iron oxide chemistry using laser-ablation inductively-coupled mass-spectrometry (LA-ICP-MS) in order to provide a comprehensive data set of the complete paragenetic iron oxide sequence. Analyses were conducted using the Resonetics M-50-LR 193 nm excimer laser ablation system coupled to an Agilent 7700x quadrupole ICPMS at the John de Laeter Centre for Isotope Research at Curtin University. Samples were ablated in a He atmosphere (flow rate 0.68 L/min) and the aerosol mixed with Ar (flow rate 1 L/min) and N (flow rate 0.0028 L/min) carrier gas for transport to the ICP-MS. Laser energy was 100 mJ with a 75 µm spot size, pulse frequency of 7 hz with 46% attenuation and fluence of 7 J/cm2. The ablation time

was 30 s with a dwell time of 0.01 s. The sample was ablated to a depth of approximately 30 μm. The GSD-1G, GSE-1G and NIST-610 standards from USGS were ablated in duplicate at the beginning of each sample analysis, every 20 spots, and at the end of each analysis, for calibration and drift correction. The following isotopes were measured: ^{24}Mg, ^{27}Al, ^{28}Si, ^{31}P, ^{44}Ca, ^{45}Sc, ^{49}Ti, ^{51}V, ^{52}Cr, ^{55}Mn, ^{59}Co, ^{60}Ni, ^{65}Cu, ^{66}Zn, ^{71}Ga, ^{74}Ge, ^{75}As, ^{88}Sr, ^{89}Y, ^{90}Zr, ^{92}Zr, ^{93}Nb, ^{95}Mo, ^{118}Sn, ^{121}Sb, ^{137}Ba, ^{139}La, ^{140}Ce, ^{141}Pr, ^{146}Nd, ^{147}Sm, ^{153}Eu, ^{157}Gd, ^{163}Dy, ^{165}Ho, ^{166}Er, ^{172}Yb, ^{175}Lu, ^{182}W, ^{208}Pb, ^{209}Bi, ^{232}Th, ^{238}U. The counts per second data generated were reduced with the SILLS program (Guillong et al., 2008). Iron was used as the internal standard element using the stoichiometric Fe contents of magnetite and hematite (723691 and 699530 ppm respectively). The results and the summary statistics are provided in the Appendix B.

3.3. Fluid inclusion studies

The samples chosen for microthermometry are from the Piçarrão-Liberdade iron deposit (samples Vp1, Vp2, Vpe), the Morro Escuro ridge (samples Vmi, Vms) and the Ponte da Raiz pegmatite (sample Vb) (Table 1). Six doubly polished 100- to 200-μm-thick sections of quartz and two of beryl were examined petrographically and selected for microthermometric analysis. Detailed petrographic description and mapping were undertaken using a Leica petrographic microscope to discriminate fluid inclusions (FIs) types (Table 2), sizes, morphologies and definition of fluid inclusion assemblages (FIAs).

Heating and freezing experiments on fluid inclusions were conducted using a fully automated Linkam THMSG600 heating and freezing stage with a TMS 93 temperature controller at the Laboratory of Metallogeny, Institute of Geosciences, at the Federal University of Minas Gerais, Brazil. The stage was calibrated between −56.6 °C and 374.1 °C with synthetic fluid inclusion standards supplied by Linkam (pure H_2O and mixed H_2O–CO_2). The cyclic technique (Goldstein and Reynolds, 1994) was used to acquire better precision in measurements of transition of temperature between carbonic phases.

The accuracy of the freezing measurement runs is about ± 0.1 °C, and for heating runs ± 1 °C between 200 and 500 °C. Final ice melting (Tmice), clathrate melting (Tclath), total homogenization (Thtot), CO_2 homogenization ($ThCO_2$) and halite melting (Tmhal) temperatures were measured during the freezing and heating cycles, and are provided for each FI assemblage (Table 3). It was not possible to definitely determine the temperature of the eutectic melting temperature (Te), and the observations have been omitted from the table; however, the estimation of the Te of H_2O-NaCl (–21.2°C) was used to discriminate the presence of other cations besides NaCl. The CO_2 melting temperature ($TmCO_2$) is used to identify the presence of other volatiles besides CO_2 and H_2O. The microthermometric results are compiled in Table 3.

Due to the lack of independent geothermometric data for the studied veins, it was not possible to

calculated isochores and apply pressure corrections to homogenization temperatures. Since no boiling evidence was described, the homogenization temperatures measured are considered as the minimum trapping temperature.

Apparent salinity has been reported in equivalent percentage weight of NaCl (% wt. $NaCl_{eq}$). Calculations of salinity and bulk CO_2 fractions (XCO_2) were made using the MacFlinCor program (Brown and Hagemann, 1995). Equations of state by Bodnar and Vityk (1994) were applied for the H_2O-NaCl system, and by Bowers and Helgeson (1983) for the H_2O-NaCl-CO_2 system.

Individual inclusions trapped in quartz from the Vp1, Vp2, Vpe, Vmi and Vms veins (Tables 1, 2) were analyzed by (LA-ICP-MS). These analyses were completed at the Laser Ablation ICP-MS laboratory at the University of Leeds, England. The samples were introduced into the sample chamber of the ArF 193-nm excimer laser Geolas Q Plus and were analyzed in steps of 300 s, during which several inclusions were opened by the laser ablation process (30 μm spot size). The entire content of inclusions extracted was transported as an aerosol together with He gas. The samples were then analyzed by ICP-MS Agilent 7500c quadrupole, equipped with an octopole reaction cell. The analyses were calibrated using the NIST SRM 610 standard. The data collected from the ICP-MS were processed by the software SILLS (Guillong et al., 2008), for calibration, background correction and floating of the integration signal. During this procedure, to ensure that the fluid inclusion signals were being processed without the interference of the host crystal, only spectra containing signals coincident with Na and other cations were processed. The results are presented as the weight ratios relative to Na (internal standard element) for each inclusion analyzed. The element/Na ratios were converted into absolute concentrations in ppm using a charge-balance relationship against Cl^- concentrations (Allan et al., 2005), which was estimated from microthermometric measurements as described above. The average salinity of fluid inclusions in the FIA was used for the determination of Cl^- concentration instead of the individual salinities.

4. Geological setting of itabirite hosted Fe deposits

In this section, we provide descriptions of three itabirite sequences in terms of geological setting, mineralogy and veins type. These are (1) Liberdade-Piçarrão; (2) Morro Escuro; and (3) Dores de Guanhães and Guanhães (Figs. 1 and 2).

4.1. Piçarrão-Liberdade deposit

The Piçarrão-Liberdade deposit is hosted by an itabirite-bearing metasedimentary sequence comprising quartz schist and sillimanite-bearing banded paragneiss. Pegmatite veins composed of quartz, K-feldspar and plagioclase (Vpe, see Table 1) cut the sequence. The deposit is located close (< 1 km) to the contact between the metasedimentary sequence with the Borrachudos

granite (Fig. 2).

The itabirite forms strongly folded and deformed lenticular bodies intercalated within biotite-quartz schist, and quartz-rich, sillimanite-garnet-biotite gneiss that strike 5 km in the NE direction. The banding of the itabirite (Fig. 3a) is flat lying to gently dipping (10°-15° NW), presents tight folds and is partially transposed. Two types of quartz veins are hosted in the itabirite: (1) concordant quartz veins, and (2) discordant quartz-martite veins (see section 4.1.2.).

High-grade iron (HGI) orebodies (~65 wt. % Fe) in itabirite are 5-30 m-thick, banded to compact, locally display foliated texture (Fig. 3c), and are locally positioned at the contact with pegmatite. Banded orebodies are rich in granoblastic hematite (Fig. 3b) and have subordinate tabular hematite, and the foliated orebodies are rich in tabular hematite (Fig. 3d) with subordinate granoblastic hematite. Compact orebodies have massive structure, and are composed of martite grains in granoblastic hematite. The shape of the high-grade orebodies is totally or partially controlled by the banding of the itabirite protore. The genesis of the high-grade orebodies is probably related to syntectonic quartz leaching by pressure solution along thrust zones during the hydrothermal overprint that affected the entire Serra do Espinhaço fold-and-thrust belt during the Brasiliano orogen (Rolim and Rosière, 2011; Rolim et al., 2016). In this context, the foliated high-grade rocks represent the most-altered and recrystallized portions of the orebodies, and the compact and banded high-grade rocks represent the least-deformed areas.

Pegmatite occurs as lenticular bodies and boudins, with variable thickness, in the entire sedimentary sequence. The pegmatites are composed of quartz, K-feldspar and plagioclase.

Specular hematite is hosted in shear zones and quartz veins as elongated grains oriented parallel to each other, defining a strong foliation.

4.1.1. Itabirite: ore mineralogy and paragenesis

The dominant iron oxide in the itabirite is lamelar hematite, forming mesobands with quartz and idiomorphic martite (martite-I) crystals (~250 μm) overprinted by lamelar hematite (~330 μm) (Fig. 4a). Relicts of kenomagnetite (kenomagnetite-I) represent the earliest iron oxide, enclosed in martite-I and rarely in hematite in the itabirite (Figs. 4c, 5). Kenomagnetite is formed during the oxidation of the magnetite. This process involves mobilization of Fe^{2+} ions and their removal from the system, resulting in a relative Fe^{+2} -poor kenomagnetite. The result of this process produce martite crystals, which are pseudomorphs of magnetite with hematite composition.

The high-grade iron ore is composed of granoblastic and tabular hematite, and 10 to 30% of martite-I (Figs. 4b, 4d) with a strong intragranular porosity. Kenomagnetite-I appears as relicts within martite-I grains. Banded high-grade orebodies are enriched in granoblastic hematite, whereas foliated, high-grade orebodies are enriched in tabular hematite. Granoblastic hematite overprints martite-I, itself overprinted by tabular hematite (Figs. 4c, 4d). Compact high-grade ore is

composed of martite-I that is not overprinted by new crystals of hematite.

A second generation of magnetite crystallized/precipitated during the formation of the discordant quartz-martite-II veins (Vp2). The oxidation of this magnetite generated the subhedral martite-II crystals with a well-developed octahedral cleavage. The martite-II crystals are preserved from the metamorphic recrystallization that formed granoblastic hematite from martite-I within high-grade orebodies and itabirite. Kenomagnetite-II appears as relicts within martite-II grains (Figs. 4e, 5, 6a).

4.1.2. Vein types

Three quartz-bearing vein types are identified at the PLD (Fig. 6a and Table 1): Vp1 - quartz-only vein hosted in high-grade orebodies; Vp2 - quartz-martite-II veins; and Vpe quartz-K-feldspar-plagioclase pegmatitic veins.

The Vp1 shows a sharp contact with the host rock and is folded with banding. Quartz (Qtz1) is fine to medium-grained, strongly fractured, with undulose extinction. This vein type varies from 2 to 5 cm in thickness. The Vp2 is hosted in itabirite, mostly discordant, crosscutting the itabirite foliation. It seems to develop a hematite enrichment halo in the contact with itabirite (Fig. 6a). The Vp2 is composed of medium to coarse-grained, subhedral quartz (Qtz2) with undulose extinction and martite-II. This vein type varies from 2 to 30 cm in thickness. The relationship of Vp1 and Vp2 with their host rock structures indicates that Vp1 vein is older than Vp2. The Vpe crosscuts the granite in the deposit area. It is composed of quartz-Qtz3 (40%), K-feldspar (30%) and plagioclase (30%) with hypidiomorphic texture. The Vpe thickness varies from 1 to 5 cm; its relation to Vp1 and Vp2 is not clear.

4.2. Morro Escuro ridge

The Morro Escuro (ME) ridge is an allochthonous shear zone-bound block that strikes 7 km in the NE-SW direction, located between slices of the Archean Basal Complex and the Paleoproterozoic Borrachudos Suite (Carvalho et al., 2014) (Fig. 2).

The Morro Escuro ridge supracrustal rocks were subdivided by Braga et al. (2015) in four lithostratigraphic units: (1) biotite schist, (2) lower and (3) upper quartzite and (4) itabirite. The itabirite unit occurs as NE-SW-striking layers with 15-60 m thickness, in gradational contact with 4 m thick ferruginous quartzite (Fig. 6b). Morro Escuro ridge lacks significant high-grade iron mineralization, and the itabirite Fe grade varies from 30 to 35 wt. %.

4.2.1. Itabirite mineralogy and paragenesis

Itabirite has a schistose fabric containing lamelar hematite crystals with irregular intergrowths and

martite-I. Kenomagnetite-I appears as relicts in martite-I, or as subhedral crystals grown in a fine-banded lamelar hematite matrix in the itabirite (Fig. 5).

Small (<1 m thick), high-grade iron lenses consists of tabular-granoblastic hematite with strong intragranular porosity to compact granular kenomagnetite-I. Banded, high-grade lenses are enriched in granoblastic hematite, whereas foliated, high-grade lenses are enriched in tabular hematite. Granoblastic hematite overprints kenomagnetite-I, and is overprinted by tabular hematite. Compact high-grade lenses are composed of kenomagnetite-I that displays only minor martitization along fractures and cleavage planes and is not overprinted by hematite. Specular hematite is hosted in shear zones and quartz veins as elongated grains oriented parallel to each other, defining a strong foliation.

4.2.2. Vein types

Two types of quartz veins occur at the Morro Escuro ridge: Vmi hosted in itabirite and Vms hosted in quartz schist (Fig. 6b and Table 1). The Vmi vein is concordant to the foliation of the itabirite and is composed of medium-grained quartz with undulose extinction. The vein border is enriched in tabular hematite. The Vmi thickness varies from 1 to 3 cm (Fig. 6b). The Vms veins are boudinaged, parallel to the foliation of the quartz schist and comprise medium-grained quartz. The Vms thickness varies from 5 to 50 cm. In both Vmi and Vms, quartz crystals are highly deformed, with undulose extinction and recrystallized borders.

4.3. Dores de Guanhães (DGN) and Guanhães (GNH) prospects

The DGN prospect is located 35 km north of the Morro Escuro ridge within rocks of the Guanhães Complex (Fig. 1), and less than 1 km from the Borrachudos Suite granite. A lens of high-grade iron strikes N-S for approximately 1 km and dips sub-vertically with an average thickness of 3 m. (Centaurus, 2014).

The GNH prospect is located on the outskirts of the town of Guanhães. The geological units consist of TTG granites of the Guanhães Complex and dolomitic itabirite of the Guanhães Group. Itabirite appears as elongated and isolated segments within the Guanhães Complex (Fig. 1); it is folded, with the fold axes of the tight to isoclinal folds plunging between NW to NE (Centaurus, 2014).

4.3.1. Itabirite mineralogy and paragenesis

The dominant iron oxides in the banded high-grade iron lens at the DGN are granoblastic hematite and martite-I crystals in fine-grained goethite. Hematite overprints martite-I. Small (<10 cm) lenses

of compact high-grade iron bodies occur at GNH where the dominant iron oxide is kenomagnetite-I locally overprinted by granoblastic hematite. Small (<10 cm) lenses of foliated high-grade iron bodies are composed of tabular hematite with subordinate granoblastic hematite.

5. Whole rock geochemistry

5.1. Piçarrão-Liberdade deposit

Itabirite at the PLD consists mainly of Fe_2O_3 (52.9 wt. %) and SiO_2 (45.7 wt. %), with minor Al_2O_3 (0.2 wt. %). The Fe_2O_3 content of high-grade iron orebodies varies from 95 to 99 wt. %, with higher concentrations of Al_2O_3 (0.4 – 0.8 wt. %). The compact sample is the most enriched in martite and kenomagnetite, and it shows the highest FeO content (12.8 wt. %). The foliated, hematite-enriched samples present the lowest FeO content (1.2 and 4.2 wt. %) (Appendix A).

Normalized to the PAAS-(sn) (Post-Archaean Average Australian Sedimentary Rocks; McLennan, 1989), the itabirite REE + Y spidergram (Fig. 7) shows the typical HREE enrichment in relation to LREE, $Pr/Yb_{(sn)}$ = 0.31. The itabirite has a slight negative $Eu_{(sn)}$ anomaly (Eu/Eu* = 0.89), presents seawater-like Y/Ho ratios (> 40) (Fig. 8), and a positive $Ce_{(sn)}$ anomaly (Fig. 9). The chondrite-normalized (Taylor and McLennan, 1985) $Eu_{(cn)}$ anomaly is negative ($Eu/Eu^*_{(cn)} = Eu_{(cn)}/0.5Sm_{(cn)} + 0.5Gd_{(cn)}$= 0.62).

The banded sample shows anomalous enrichment in LREE, which is probably the result of supergene alteration (goethite enrichment), and subsequently not further discussed. Although foliated and compact samples present REE pattern similar to the itabirite, the foliated samples show depletion in LREE content, whereas the compact sample presents slight enrichment in REE content (Fig. 7). The foliated samples are also slightly enriched in V, Pb, Ni, Co, As and Hg; when compared to the itabirite.

5.2. Morro Escuro ridge

Two samples of itabirite from Morro Escuro ridge were analyzed; one from the SW extension and the other from the NE extension (Fig. 2). The major elements abundances for these two samples are very similar. Itabirite at the Morro Escuro ridge consists mainly of Fe_2O_3 (55 - 56 wt. %) and SiO_2 (42 – 45.5 wt. %), with minor Al_2O_3 (0.13 – 0.26 wt. %). High-grade banded lenses contain Fe_2O_3 (77.8 wt. %) and SiO_2 (19.7 wt. %), with higher concentrations of Al_2O_3 (0.5 wt. %). Foliated lenses have higher concentrations of Fe_2O_3 (99.1 wt. %) and is enriched in Al_2O_3 (1.29 wt. %). Compact samples are the most enriched in martite and kenomagnetite, they show the highest FeO content (6.5 and 9.5 wt. %) (Appendix A).

Normalized to the PAAS (McLennan, 1989), the two itabirite REE + Y spidergrams (Fig. 7) present

different LREE/HREE ratios ($Pr/Yb_{(SN)}$ = 1.25 and 0.31). Both itabirites have positive a $Y_{(sn)}$ and $Eu_{(sn)}$ anomaly (Eu/Eu* = 1.44 and 1.34), present signatures of terrigenous input (shale field), as indicated by the low values of Y/Ho (under 35) (Fig. 8), and are HREE depleted. One itabirite presents a positive $Ce_{(sn)}$ anomaly (Fig. 9), similar to the Ce-allanite itabirite of Braga et al. (2015). The chondrite-normalized (Taylor and McLennan, 1985) $Eu_{(cn)}$ anomaly is close to 1.00 ($Eu/Eu^*_{(cn)}$ = 0.96 and 0.89). The foliated sample shows very pronounced HREE enrichment and slight enriched in Cr, Sr and V. In relation to the itabirite, the foliated and compact samples show slight depletion in REE content (Fig. 7).

5.3. Dores de Guanhães (DGN) and Guanhães (GNH) prospects

Dolomitic itabirite at GNH consists mainly of Fe_2O_3 (53.5 wt. %) and SiO_2 (44.8 wt. %), with minor MgO (0.07 wt. %). High-grade samples at DGN and GNH consist of Fe_2O_3 (95.6 to 97.9 wt. %) with variable concentrations of Al_2O_3 (0.1 to 1.24 wt. %). The compact sample is the most enriched in martite and kenomagnetite, and shows the highest FeO content (20.7 wt. %) (Appendix A).
Normalized to the PAAS (McLennan, 1989), the itabirite REE + Y spidergram (Fig. 7) shows the typical HREE enrichment in relation to LREE, $Pr/Yb_{(sn)}$ = 0.42. The itabirite sample from GNH have a positive $Eu_{(sn)}$ anomaly (Eu/Eu* = 1.77), and presents a signature for a terrigenous input (shale field), indicated by the low values of Y/Ho (under 35) (Fig. 8). The chondrite-normalized (Taylor and McLennan, 1985) $Eu_{(cn)}$ anomaly is also positive ($Eu/Eu^*_{(cn)}$ = 1.22). In relation to the itabirite, the foliated and compact samples show depletion in REE content, and the banded sample presents enrichment in REE content (Fig. 7). Compact and foliated samples are enriched in As and Pb, whereas banded sample is enriched in As, Cr, Pb and Sr.

6. Iron oxide LA-ICP-MS studies

6.1. Piçarrão-Liberdade deposit

Itabirite-bearing kenomagnetite-I and lamelar hematite show similar chemical patterns with considerable amounts of Al (1100-1200 ppm), Ti (80-120 ppm), V (30-35 ppm) and Cr (5-10 ppm). Second-stage martite-II in quartz-martite-II veins contains mainly Mg (625 ppm), Al (861 ppm), P (156 ppm), V (40 ppm), Cr (10 ppm) and Mn (1004 ppm). Other trace elements such as Ti, Co, Ni, Zn, Ga, As and Mo have concentrations of <5 ppm. The REE concentrations of martite-II (Vp2) are the highest of all other iron oxides (Fig. 10), and its PAAS-normalized diagram exhibits slight HREE enrichment and positive Ce anomaly (Fig. 11a, Appendix B).
Kenomagnetite-I in high-grade orebodies contains high amounts of Mg (697 ppm), Al (743 ppm), V (55 ppm), Cr (15 ppm) and Mn (815 ppm). In relation to itabirite iron oxides, kenomagnetite-I is

enriched in all elements except Al, Ti and Mo, REE are below the detection limits. Martite-I alteration of kenomagnetite-I is accompanied by significant depletions in Mg, Ti, V, Cr, Mn, Co and Ni with enrichment in Al, P and As. The PAAS-normalized diagram for martite-I exhibits HREE enrichment and positive Ce anomaly (Figs. 10 and 11a).

Granoblastic hematite contains mainly Al (819 ppm), P (18 ppm), Ti (81 ppm), V (39 ppm), and Cr (29 ppm). Other trace elements such as Mg, Co, Ni, Zn, Ga, As and Mo have concentrations <5 ppm, and together with Mn are depleted in relation to paragenetically older martite-I, whereas Mo, Ti and Cr are enriched. No REE >1 ppm were detected. Paragenetically younger tabular hematite is less abundant than granoblastic hematite in P, Ti, Cr, and Mn, whereas Al, V, Ga and Mo are relatively enriched. Shear zone- and vein-hosted specular hematite is significantly depleted in most trace elements and REE, containing only Al (399 ppm) and V (6 ppm) in significant amounts.

6.2. Morro Escuro ridge

Martite-I of the least altered itabirite represents the paragenetically earliest oxide at Morro Escuro ridge, and has considerable amounts of Mg (56 ppm), Al (845 ppm), P (564 ppm), V (33 ppm), Cr (6 ppm), Mn (17831 ppm), Co (31 ppm), Ni (164 ppm), Zn (129 ppm), Ga (5 ppm), and As (15 ppm). Other trace elements such as Ti and Mo, as well as REE, are not present in concentrations >2 ppm other than Ce (3 ppm) and Y (3 ppm). The REE concentrations are the highest in all other iron species, and the PAAS-normalized diagram for martite-I exhibits HREE enrichment and positive Ce anomaly (Figs. 12 and 11b). Paragenetically younger lamelar hematite is depleted in most trace elements and REE other than Al, V and Cr, and enriched in Ti (142 ppm).

Kenomagnetite-I in high-grade orebodies contains mostly Mg (26 ppm), Al (66 ppm), P (37 ppm), V (94 ppm), Mn (1106 ppm), Ni (11 ppm), and Zn (129 ppm) with other trace elements and REE present in concentrations <5 ppm. Relative to paragenetically younger kenomagnetite-I, tabular hematite is depleted in Mn, Co, Ni, Zn; and enriched in Al (3694 ppm), Ti (1967 ppm), Cr and Mo.

Compact kenomagnetite-I in high-grade orebodies has high concentrations of Mg (24679 ppm), significant amounts of Al (1359 ppm), Ti (117 ppm), V (75 ppm), Cr (9 ppm), Mn (3627 ppm), Ni (7 ppm) and Zn (7 ppm); concentrations of other trace elements and REE do not exceed 2 ppm. Relative to kenomagnetite-I overprinted by tabular hematite, compact kenomagnetite-I is enriched in Mg, Al, Ti, and depleted in P and Zn. Shear zone- and vein-hosted specular hematite is characterized by Al (696 ppm), P (9 ppm), Ti (42 ppm), V (37 ppm) and Mn (15 ppm). Other elements such as Mg, Cr, Co, Ni, Zn and REE were not detected in concentrations >2 ppm.

6.3. Dores de Guanhães (DGN) and Guanhães (GNH) prospects

Kenomagnetite-I from banded, high-grade lens represents the earliest paragenetically iron oxide

species at GNH. It is characterized by high concentrations of Mg (38545 ppm), and considerable Al (1838 ppm), Ti (19 ppm), V (56 ppm), Cr (32 ppm), Mn (4215 ppm), Co (29 ppm), Ni (68 ppm), Zn (8 ppm) and Ga (7 ppm) (Fig. 13). Arsenic and Mo as well as REE were not present in concentrations >1 ppm. Paragenetically younger granoblastic hematite is relatively depleted in Mg, Mn, Co, Ni, Zn and Ga when compared to kenomagnetite-I, and enriched in Ti (2635 ppm) and Mo. compact kenomagnetite-I is depleted in P, Cr, Co and Ni in relation to kenomagnetite-I from banded, high-grade lens.

Granoblastic hematite from banded, high-grade lens at DGN is relatively depleted in Mg and Ti when compared to granoblastic hematite from GNH, and enriched in P, Cr and Ga. Martite-I from banded, high-grade lens at DGN is relatively enriched with respect to most trace elements when compared to granoblastic hematite at DGN, other than Al (3750 ppm) (Fig. 12). The REE are slightly enriched, and the PAAS-normalized diagram for martite-I exhibits HREE enrichment and positive Eu anomaly (Fig. 11c).

7. Fluid inclusion studies at the Piçarrão-Liberdade (PLD) iron deposit, the Morro Escuro ridge itabirite sequence and the Ponte da Raiz beryl-bearing pegmatite

The samples used in the fluid inclusion studies at PLD and ME areas were selected according to the vein classification in sections 4.1.2. and 4.2.2. In the following sections the areas selected for microthermometry are described in terms of its fluid inclusions content (Figs. 14, 15, 16, 17).

7.1. Fluid inclusions trapped in quartz from the Piçarrão-Liberdade (PLD) iron deposit

Vein samples from itabirite (40% Fe), high-grade iron ore (>55%Fe) and gneiss were chosen from the PLD for microthermometry and LA-ICP-MS analyses (Table 2).

7.1.1. Fluid inclusions types and assemblages

7.1.1.1. Vp1 veins

The Qtz1 crystals from the quartz vein in the high grade iron ore (Vp1; Figs. 5 and 6) host fluid inclusion assemblages that form three-dimensional clusters and trails They are interpreted as pseudosecondary in nature because of the confinement of the cluster and trails to individual crystal (Roedder, 1984) (Fig. 14a). Secondary trails of inclusions are also observed, but not considered here for data interpretation due to their unclear relationship with the mineralization process. According to the number, nature, and volume proportions of phases present at room temperature, two types of fluid inclusion are classified in these Qtz1 crystals: Type 1, two-phase (L-V) aqueous;

and type 2, four-phase (L-L-V-S) aqueous-carbonic (Fig. 14f) with aqueous-saline phase, liquid CO_2, vapor and solid phases (daughter crystals).

Type 1 FIs have a high liquid/vapor ratio (average 85% liquid, 15% vapor), and form irregularly shaped to rounded inclusions in secondary trails. Type 2 FIs have highly variable H_2O/CO_2 ratio (volume fraction of CO_2 varies from 30 to 80 vol. %), average size between 25-35 ⌈m and form irregularly shaped to rounded inclusions. Locally, negative crystal shape was observed in type 2 inclusions.

7.1.1.2. Vp2 veins

Coarse-grained Qtz2 crystals from the itabirite-hosted quartz-martite-II veins (Vp2; Figs. 5 and 6) contain only type 1 two-phase (L-V) aqueous FIs, with constant L/V ratios (5-15% vapor) and smaller average size (10-20 ⌈m) than Qtz1 FIs. These type 1 FIs are irregularly shaped to rounded inclusions, form three-dimensional clusters and internal trails, and are interpreted as pseudosecondary inclusions (Fig. 15). Secondary trails of inclusions are also observed, but not considered here for data interpretation due to their unclear relationship with the mineralization process.

7.1.1.3. Vpe veins

The Qtz3 crystals from the granite-hosted pegmatite vein (Vpe; Fig. 6) share some similarities with Qtz2 in terms of their FIs content and contain only type 1, two-phase (L-V) aqueous FIs, with more constant L/V ratios (5-15% vapor), and average size between 10-20 ⌈m. These type 1 FIs form three-dimensional clusters and/or internal trails and are interpreted as pseudosecondary (Fig. 16).

7.1.2. Microthermometry

7.1.2.1. Vp1 veins

Freezing experiments on the CO_2-rich assemblages (type 2 FIs) demonstrate that the nine fluid inclusion assemblages have internally consistent eutectic temperatures (Te) that range from - 30 to - 39 °C, suggesting other cations besides Na. Melting temperatures of clathrate (Tclath) define a maximum ranging from 7.5 to 9.0 °C (Table 3). Within fluid assemblages Tclath determinations vary by 0.8 °C. The formation of hydrohalite crystals was observed during the freezing experiments, between -8 and -1 °C. Melting temperatures of CO_2(s) - $TmCO_2$ - are between −57.9 to −56.6 °C, suggesting CO_2 to have been the most abundant gas species. The bulk CO_2 fraction (XCO_2) varies from 0.1 to 0.54 (H_2O – 0.9 to 0.46), and the CO_2-rich phase homogenized ($ThCO_2$)

over a wide range of temperatures, from 25 to 31.5 °C.

Type 2 inclusion assemblages homogenize by the disappearance of liquid-(CO_2) over a wide range of temperatures, from 270 to 373 °C although ThTot values for individual fluid inclusion assemblages vary only by 15 °C (Table 3). Inclusions with the highest content of CO_2 (XCO_2) present the highest ThTot. These ThTot data represent a minimum trapping temperature since no boiling evidence was observed. Two types of solid phases (daughter crystals) were observed, sylvite and halite. Sylvite crystals are slight pleochroic (Fig. 14f) and dissolve between 15 and 35 °C. Halite appears as non pleochroic square shaped crystals with higher dissolution temperatures between 70 and 87 °C. The salinity values display small variations between 26.5 to 27.6 wt. % NaCl equiv. (Fig. 18), and was calculated based on the halite dissolution temperature (Tmhal).

7.1.2.2. Vp2 veins

Freezing experiments on type 1 two-phase (L-V) aqueous FIs demonstrate that the seven fluid inclusion assemblages have internally consistent eutectic temperatures (Te) that range from -30 to -40 °C, suggesting other cations besides Na. Melting temperatures of ice (Tmice) are variable and define a maximum Tmice ranging from -0.7 to -8.5 °C (Fig. 18). Within fluid assemblages Tmice determinations vary by 3 °C. Type 1 inclusion assemblages homogenize by the disappearance of vapor bubbles over a wide range of temperatures, from 144 to 260 °C, although ThTot (L) values for individual fluid inclusion assemblages vary only by 20 °C (Table 3).

7.1.2.3. Vpe veins

Freezing experiments on type 1 two-phase (L-V) aqueous FIs demonstrate that the three fluid inclusion assemblages have internally consistent eutectic temperatures (Te) that range from -30 to -40 °C, suggesting other cations besides Na. Melting temperatures of ice (Tmice) are variable and define a maximum Tmice ranging from –2.1 to –6.1°C (Fig. 18). Within fluid assemblages Tmice determinations vary by 1.6 °C. Type 1 inclusion assemblages homogenize by the disappearance of vapor bubbles over a wide range of temperatures, from 156 to 348 °C, although ThTot (L) values for individual fluid inclusion assemblages vary only by 55 °C (Table 3).

7.1.3. Quantitative estimation of fluid inclusion composition based on LA-ICP-MS data

Analytical results for inclusions from Vp1, Vp2 and Vpe veins show that Na, K, Ca and Fe are the dominant components (Table 4). Type 1 two-phase (L-V), aqueous FIs were analyzed in Qtz2 from Vp2 veins, and in Qtz3 from Vpe vein; and type 2 four-phase (L-L-V-S) aqueous-carbonic FIs were analyzed in Qtz1 from Vp1 vein.

Fluid inclusions trapped in Qtz1 (Vp1 veins) are enriched in Ca (av. Ca/Na = 0.514), Mn, Cu, Zn, Pb, Sr and Ag when compared to Qtz2 and Qtz3 (Table 4, Fig. 19). Only 1/3 of the analyzed FIs show Fe above the limit of detection, but for these FIs the Fe concentration is high. Bivariate and ternary diagrams (Fig. 20) show good correlation between Cu versus Zn and Sr versus Ca, but no correlation of Fe with other major components, such as K or Ca.

Fluid inclusions trapped in Qtz2 (Vp2 veins) are rich in K and Fe relative to Na (K/Na = 1.44; Fe/Na = 0.418). The Fe concentration is high, similar to type 2 FIs trapped in Qtz1 (Table 4, Fig. 19). The other analyzed cations show very low values that are close to the limit of detection. Bivariate diagrams of Zn versus Cu and Sr versus Ca show good correlation, but in the Fe versus K diagram there is a wide dispersion in data.

Fluid inclusions trapped in Qtz3 (Vpe veins) are rich in K relative to Na (K/Na = 0.676). As well as Qtz1, the Cu, Zn and Li element ratios are high in FIs trapped in Qtz3 (Table 4, Fig. 19). Other analyzed cations show very low values, close to the limit of detection.

7.2. Fluid inclusions trapped in quartz from the Morro Escuro ridge

From the Morro Escuro ridge, vein samples from itabirite (40% Fe) and quartz schist were chosen for microthermometry and LA-ICP-MS analyses (Table 2).

7.2.1. Fluid inclusions types and assemblages

7.2.1.1. Vmi veins

The Qtz1a crystals from the quartz vein in the itabirite (Vmi) host fluid inclusion assemblages that form three-dimensional clusters and internal trails. They are interpreted as pseudosecondary because of the confinement of the cluster/trails to individual crystals according to criteria proposed by Roedder (1984) (Fig. 17b). No FIs are observed in recrystallized quartz crystals. Secondary trails of inclusions are also observed, but are not considered here for data interpretation due to their unclear relationship with the mineralization process.

According to the number, nature, and volume proportions of phases present at room temperature, two types of fluid inclusion are classified in these Qtz1a crystals: Type 1 two-phase (L-V) aqueous; and type 2 four-phase (L-L-V-S) aqueous-carbonic with aqueous-saline phase, liquid CO_2, vapor and solid phases (daughter crystals). Type 1 FIs have a high liquid/vapor ratio (average 85% liquid, 15% vapor) and form irregularly shaped to rounded inclusions in separate assemblages (FIA 24 – Table 3). Type 2 FIs have highly variable H_2O/CO_2 ratio (volume fraction of CO_2 varies from 30 to 80 vol. %), average size between 35-45 ⌈m, and are irregularly shaped to rounded inclusions. Type 2 inclusions locally display a negative crystal shape.

7.2.1.2. Vms veins

The Qtz1a crystals from the quartz vein in the quartz schist (Vms) host fluid inclusions assemblages that form three-dimensional clusters and internal trails. They are interpreted as pseudosecondary because of the confinement of the cluster/trails to individual crystal according to criteria by Roedder (1984) (Fig. 17d). Secondary trails of inclusions are also observed, but are not considered here for data interpretation due to their unclear relationship with the mineralization process. Three types of FIs are defined in Vms veins (Table 2): Type 1 two-phase (L-V) aqueous; type 2 four-phase (L-L-V-S) aqueous-carbonic with aqueous-saline phase, liquid CO_2, vapor and solid phases (daughter crystals), and type 3 three-phase, (L-L-V) aqueous-carbonic with aqueous-saline phase, liquid CO_2, and vapor.

7.2.2. Microthermometry

7.2.2.1. Vmi veins

Freezing experiments on aqueous (type 1 FIs) and CO_2-rich (type 2 FIs) assemblages demonstrate that the fluid inclusion assemblages have internally consistent eutectic temperatures (Te) that range from −38 to −45 °C, suggesting the presence of other cations besides Na. Melting temperatures of ice (Tmice) of one type 1 two-phase (L-V) aqueous fluid assemblage have a maximum Tmice of -1.8 °C that vary by 0.6 °C. This type 1 inclusion assemblage homogenizes by the disappearance of vapor bubbles at 145 °C (Table 3). This data represents a minimum trapping temperature since no boiling evidence was observed.

Melting temperatures of clathrate (Tclath) of four CO_2-rich fluid inclusion assemblages define a maximum ranging from 7.6 to 8.2 °C (Table 3). Within fluid assemblages Tclath determinations vary by 3 °C. All the measured melting temperatures of CO_2(s) ($TmCO_2$) are coincident at −56.6 and °C, suggesting that CO_2 is the most abundant gas species. The bulk CO_2 fraction (XCO_2) varies from 0.03 to 0.3, and the CO_2-rich phase homogenize ($ThCO_2$) from 22.4 to 32 °C. These type 2 inclusion assemblages homogenize by the disappearance of liquid-(CO_2) over a wide range of temperatures, from 290 to 340 °C, and ThTot values for individual fluid inclusion assemblages vary by 20 °C (Table 3). Inclusions with the higher content of CO_2 (XCO_2) present the highest ThTot. These ThTot data represent a minimum trapping temperature since no boiling evidence was observed. The dissolution temperatures of the solid phases are between 20 and 30 °C for sylvite crystals and between 35 and 58 °C for halite crystals. The salinity values display small variations between 26.6 to 26.9 wt. % NaCl equiv. (Fig. 18), and were calculated based on halite dissolution temperature (Tmhal).

7.2.2.2. Vms veins

Freezing experiments demonstrate that the 26 fluid inclusion assemblages have internally consistent eutectic temperatures (Te) that range from −38° to −45 °C, suggesting the presence of other cations besides Na. Melting temperatures of ice (Tmice) are variable and define a maximum Tmice ranging from –2.5 to –11 °C. Individual fluid assemblages have Tmice determinations that vary by 1 °C. These type 1 inclusion assemblages homogenize by the disappearance of vapor bubbles over a low range of temperatures, from 130 to 140 °C. These ThTot data represent a minimum trapping temperature since no boiling evidence is observed.

Melting temperatures of clathrate (Tclath) of five CO_2-rich fluid inclusion assemblages define a maximum ranging from 5.0 to 9.3 °C (Table 3). Within fluid assemblages Tclath determinations vary by 2 °C. All the measured melting temperatures of CO_2(s) ($TmCO_2$) are coincident at −56.6 and °C, suggesting that CO_2 is the most abundant gas species. The CO_2-rich phase homogenizes ($ThCO_2$) over a wide range of temperatures from 15 to 31 °C. These types 2 and 3 inclusion assemblages homogenize by the disappearance of liquid-(CO_2) over a low range of temperatures, from 220 to 250 °C, and ThTot values for individual fluid inclusion assemblages vary by 10 °C (Table 3). The solid phases in type 2 FIs (sylvite and halite) have similar dissolution temperatures as type 2 FIs of the Vmi veins. The salinity of type 2 FIs was calculated based on halite dissolution temperature (Tmhal), and the salinity of type 3 FIs based on clathrate melting (Tclath).

7.2.3. Quantitative estimation of fluid inclusion composition - LA-ICP-MS

Analytical results for inclusions from Vmi and Vms veins show that K, Na, Ca, Fe and Mg are the dominant components (Table 4). Only type 2 four-phase (L-L-V-S), aqueous-carbonic inclusion assemblages were analyzed in Qtz1a from Vmi and Vms veins. Both Vmi and Vms veins show K as the main cation component, and similar values of Na and Ca concentrations. Relative to Vms, FIs trapped in Qtz1a from Vmi has higher concentration of Fe, and lower concentration of Mg and Zn.

The bivariate diagrams (Fig. 21), show good correlation between Ca versus Sr, Cu versus Zn and Ca versus K. Compared to the PLD, FIs data from ME veins shows small variations in the ternary diagrams Fe-K-Ca and Fe-K-Mg, and the relation between the main components K and Na is inverted; K>Na at ME and Na>K at PLD (Figs. 19 and 21). The same trend in the Fe-Cu-Zn diagram is observed in both PLD and ME.

7.3. Fluid inclusions trapped in beryl from the Ponte da Raiz pegmatite

7.3.1. Fluid inclusions *types and assemblages*

Fluid inclusions were studied in two beryl samples, Be1 and Be2, both from the Ponte da Raiz pegmatite (Table 2). Beryl-(Be1) is green and contains abundant fluid inclusion. Three types of inclusions are described, all with the same composition at room temperature – aqueous-carbonic, four-phase (L-L-V-S) with aqueous-saline phase, liquid CO_2, vapor and halite daughter crystals. Halite daughter crystals were identified by dissolution temperature and square shape. However, these three types present distinct shapes and orientation with respect to the beryl crystallographic axes (Fig. 17f): Type 2a FIs show tubular shape and is interpreted to be primary because they are always oriented parallel to some of the crystallographic axes. Type 1 is the most abundant in number and volume. Type 2b FIs show tabular-rounded shape, are the largest (>50 μm), and are associated with pseudosecondary trails that do not cross the crystal boundaries. Type 2c FIs show square shape, are smaller than Type 2, and form pseudosecondary clusters inside the crystal. Beryl-(Be2) is light yellow and has rare FIs. Only Type 2c FIs are observed in Be2, but it was not possible to analyze them because they are necked.

7.3.2. Microthermometry

Eutectic temperatures (Te) estimation vary slightly from −24° to −26 °C for all inclusions assemblages on Be1, suggesting low concentrations of other cations besides Na. Freezing experiments on the CO_2-rich assemblages (types 1, 2 and 3) demonstrate that the 14 fluid inclusions analyzed have consistent melting temperatures of CO_2(s) ($TmCO_2$) that range between −57.7 to −56.6 °C, suggesting that CO_2 is the most abundant gas species. The CO_2-rich phase homogenization temperature ($ThCO_2$) also varies slightly from 28.5 to 31.4 °C. Melting temperatures of clathrate (Tclath) are variable and define a range from 4.3 to 9.2 °C, although individual fluid assemblages have Tclath determinations that vary by 1.2 °C (table 3).
Inclusion assemblages homogenize by the disappearance of liquid-(CO_2) over a low range of temperatures, from 315 to 320 °C (Table 3). These ThTot data represent a minimum trapping temperature since no boiling evidence is observed. The salinity values display small variations between 28.7-29.2 wt. % equiv. NaCl and was calculated based on halite dissolution temperature (Tmhal).

8. Discussion

8.1. Least-altered itabirite features at Piçarrão-Liberdade, Morro Escuro and Guanhães areas

The itabirite samples (Appendix A) from each area are considered the least-altered rocks in the

sequence of high-grade iron samples. Therefore, their chemistry and mineralogy are used to evaluate depositional environment features, and to compare chemical changes during itabirite iron upgrade. Metamorphic and hydrothermal alteration affected these rocks to some extent.

For example, the positive $Ce_{(sn)}$ anomaly observed in PLD itabirite and some HGI samples (Fig. 9) is probably the result of hydrothermal alteration and does not reflect the redox conditions of the depositional environment. A similar $Ce_{(sn)}$ anomaly, associated with the generation of REE-bearing minerals, was described by Braga et al. (2015) in ME itabirite. Itabirite alteration at PLD did not produce the strong $Eu_{(sn)}$ anomaly observed in ME and GNH (Fig. 7), suggesting a different composition of the hydrothermal fluids between these areas and-or redox condition of the depositional environment. Even though only one itabirite was analyzed, the different depositional environment at PLD is also supported by the lack of clastic contamination, as show by the Y/Ho ratio (Fig. 9).

The evidence of clastic contamination (low Y/Ho; Fig. 8) and the lack of negative $Ce_{(sn)}$ anomaly (Fig. 9) present in itabirite from GNH and ME areas suggest that these sediments precipitated on a shallow marine environment, with strong influence of continental input. Similar results were found in the previous studies of Morro Escuro and Guanhães itabirites (Braga et al., 2015; Barrote, 2016).

8.2. Chemical changes during itabirite iron upgrade

The chemical changes between different iron oxide species in the paragenetic sequence can be interpreted with respect to different hypogene alteration and mineralization processes. The evolution of the trace elements and REE chemistry through the paragenetic sequence can be linked to specific ore forming processes. These processes include: (1) oxidation of magnetite to martite; (2) transformation of martite to hematite; (3) recrystallization of granoblastic to tabular hematite; (4) emplacement of quartz vein-hosted specular hematite; (5) emplacement of quartz vein-hosted martite-II.

8.2.1. Oxidation of magnetite (martitization)

Chemical changes during the transformation of magnetite to martite in high-grade orebodies at the PLD deposit is accompanied by the enrichment of Al, P and As in martite-I, and depletion in Mg, V, Cr, Mn, Co, Ni and Zn when compared to the kenomagnetite-I relicts (Fig. 10 and 4c). According to Hensler et al. (2015), the removal of Fe^{2+} and Mg (and other mobile elements) in magnetite may result in the relative enrichment of the less mobile elements in martite, in this case Al, P and As. A similar chemical change is observed in magnetite-martite alteration at GNH and DGN prospects and their relative enrichment of Ti, P, As and Mo (Fig. 13).

Kenomagnetite-I from compact HGI bodies at Me and GNH, which is not associated with martite and hematite, presents a higher content of Mg, suggesting that it has the closest composition of the original magnetite in the Guanhães Group.

At the PLD deposit REE are present in very low concentrations in both kenomagnetite-I (other than Ce) and martite-I. The positive Ce PAAS-normalized anomaly displayed by martite-I indicates an oxidizing fluid, due to the preferential precipitation of Ce when oxidized from Ce^{3+} to Ce^{4+}. The same REE pattern is observed in martite-I from itabirite at the Morro Escuro ridge and martite-I from high-grade orebodies at DGN, Ce anomaly and HREE enrichment (Fig. 11b-c).

Bau (1996) discuss the behaviour of Y/Ho in magmatic and aqueous systems and defines a primitive chondrite-like “CHARAC” (from Charge and Radius Control) signature characterized by 24 < Y/ Ho < 34 and a seawater-like signature by 44 < Y/Ho < 74 (Fig. 22). The low Y/Ho ratios (<34) detected in martite-I from Morro Escuro ridge and DGN suggest the role of hydrothermal fluids in the oxidation of magnetite to martite, resetting the itabirite – seawater-like - HREE signature. A positive PAAS-normalized Eu anomaly is documented for martite-I from Morro Escuro ridge and DGN (Fig. 22); corroborating the whole rock geochemical results of Morro Escuro ridge and DGN (Fig. 7).

8.2.2. Transformation of martite to hematite in high-grade bodies

Granoblastic hematite recrystallized from martite-I from high-grade bodies at the PLD deposit is significantly enriched in Ti and Mo (and to a lesser extent Al, V and Cr); and depleted in Mg, Al, P, Mn, Co, Ni, Zn, Ga and As (Fig. 10). The REE are strongly depleted in hematite relative to martite-I (Fig. 11a). Tabular hematite recrystallized from kenomagnetite-I at Morro Escuro ridge is also enriched in Ti, Al, Cr and Mo, and depleted in Mn, Co, Ni and Zn (Fig. 12). Granoblastic hematite at the GNH prospect shows the same chemical changes when compared to kenomagnetite-I (Fig. 13).

According to Hensler et al. (2015) the exclusion of Mg and Mn during recrystallization of hematite is likely due to the poor compatibility of Mg^{2+} and Mn^{2+} in hematite in comparison to martite. Purtov and Kotel'nikova (1993) state that titanium is commonly regarded as immobile in aqueous solutions during metasomatic processes. In this case, the removal of the mobile elements result in the relative enrichment of the titanium; and others immobile elements such as Al, V, Cr and Mo (residual enrichment).

8.2.3. Recrystallization of granoblastic hematite to tabular hematite in high-grade iron bodies

The texture transformation of hematite (granoblastic to tabular) is related to the iron enrichment during the formation of the high-grade iron bodies. This transformation shows good inheritance of

mineral chemistry, suggesting an isochemical process, a continuation of the recrystallization under similar physico-chemical conditions and fluid chemistry (martite - granoblastic hematite - tabular hematite; Figs. 10, 12, 13). The same pattern is observed in all three areas.

8.2.4. Formation of vein-hosted specular hematite at PLD and ME

Vein-hosted specular hematite and paragenetically older tabular hematite from the high-grade iron bodies share a similar depletion of trace elements; indeed all trace elements and REE are even more depleted in specular hematite (Figs. 10 and 12). This suggests that specular hematite was the last iron oxide to precipitate. The REE are more likely to have been concentrated in the earlier crystallizing hematite and the fluid was depleted in these elements during the crystallization of the last generation of hematite.

8.2.5. Formation of vein-hosted martite-II at PLD

Comparison of martite-II from quartz-martite-II veins (Vp2) with martite-I from high-grade bodies shows that martite-II is enriched in Mg, P, V, Mn, and REE, but strong depleted in As. However, compared to kenomagnetite-I from HGI, martite-II presents similar trace elements content but is relatively REE enriched (Figs. 10 and 11). The low Y/Ho ratios (<34) detected in martite-II (Fig. 22) suggest the role of hydrothermal fluids in the precipitation of the original magnetite, and this Y/Ho ratios is similar to the highly evolved granite-pegmatite systems described by Bau (1996). A negative PAAS-normalized Eu anomaly (Fig. 22) also suggests significant variation in redox-sensitive Eu during the formation of the Vp2 veins, when compared to the Eu anomaly of the itabirite and HGI (REE whole rock diagram, Fig. 7). Thus, precipitation of magnetite in the Vp2 veins probably occurred in a different physico-chemical context compared to the high-grade iron bodies.

8.3. Model for the paleo fluid system

The occurrence of fluid inclusions with different proportions of CO_2 and H_2O (variable XCO_2 and CO_2 Vol%), and different homogenization temperatures (Table 3) observed within type 2 fluid inclusion assemblages trapped in Qtz1 suggest that the cooling of a homogenous fluid (Roedder, 1984; Diamond, 1990) was the major processes to explain these heterogeneous fluid chemistry and trapping conditions during Vp1 formation. On the other hand, trapping inclusions with different homogenization temperatures and salinity in Qtz2 and Qtz3 (Table 3; Fig. 18) suggests that Vp2 and Vpe veins were formed by trapping of two or more homogeneous fluids as a result of partial

mixing (Anderson et al., 1992); probably representing mixing between low-temperature, low-salinity meteoric waters and higher-temperature, higher-salinity brines (the latter fluids are possibly related to anatexis). Although the Vp1 and Vpe have different total concentrations of NaCl equiv., they have comparable element ratios (specially Cu and Zn) determine by LA-ICP-MS (Figs. 18 and 20; Table 4). The similar element ratios between FIs trapped in Vp1 and Vpe is evidence of the contribution of anatectic fluids to the Vp1 veins. Indeed, fluid inclusions trapped in beryl crystals show similar fluid inclusion phases and phase ratios (aqueous-carbonic), and overlapping temperatures as FIs trapped in Qtz1 from Vp1 veins at the PLD deposit (Table 4; Fig. 19).

The results of the FIs studies suggest that the interaction of anatectic fluids with PLD itabirite during the metamorphic event of the Brasiliano orogen led to the silica leaching and iron enrichment of the itabirite, resulting in high-grade iron orebodies. Loss of silica bands in the itabirite coincided with the local crystallization of quartz-rich veins in some parts of these high-grade iron orebodies. Silica leaching and the transformation of magnetite to hematite are probably a contemporaneous processes, and as hematite is depleted in mobile trace element (Figs. 10, 12, 13; Appendix B), the fluids that formed Vp1 veins became trace element enriched. The high temperature, salinity and trace element enrichment of the FIs trapped in Vp1 veins (Figs. 18 and 19; table 4) suggest that these veins formed as a result of the removal of quartz-rich bands from the itabirite.

Concentrations of Fe in pseudosecondary fluid inclusions trapped in Qtz1 range from 2,731 to 19,775 ppm (Table 4). These results are similar to those found by Figueiredo e Silva et al. (2013) at Carajás iron ore deposits (82–17,507 ppm Fe) and by Thorne et al. (2014) at Paraburdoo 4E Deposit, Hamersley Province (2,349-27,796 ppm Fe).

The formation of the Vp2 veins probably occurred at a lower crustal level during the mixing of the Vp1 fluids with meteoric water, and the precipitation of magnetite (transformed to martite-II) which is enriched in trace elements (Figs. 10 and 11). The low concentration of trace elements in FIs from the Vp2 veins (Fig. 19; Table 4) results from its precipitation during the crystallization of magnetite (martite-II). The low salinity and temperature of Vp2 FIs (Fig. 18), and the different redox environment for martite-II (Fig. 22) support this evolution. Also, the good correlation between trace elements ratios (Fig. 20) supports the cogenetic relation between the fluids trapped in Vp1, Vp2 and Vpe veins.

The Vmi and Vms veins at Morro Escuro ridge are related to the same event, since both present FIs with similar compositions and temperatures (Figs. 19 and 21). The metal content of FIs trapped in both Vmi and Vms veins is depleted when compared to the FIs composition trapped in Qtz1 from Vp1 veins with similar salinities and homogenization temperatures (Table 3 and 4; Figs. 19). This suggests that due to the lower silica leaching, Vmi was formed with depleted trace element content as well as lower fluid/rock ratio at ME when compared to the PLD deposit. The good correlation between the major components of the fluids (Fig. 21), also supports the low fluid/rock ratios in the

ME veins. The lack of high-grade iron orebodies at ME corroborate these conclusions.

9. Conclusions

According to the mineral chemistry of the iron oxides paragenesis, and the fluid inclusion studies in the pegmatite and quartz veins associated with the high-grade iron bodies of the PLD deposit, it is possible to conclude that:

1. In the Piçarrão-Liberdade deposit-PLD, the paragenetic sequence of the iron oxides show three major chemical trends: (i) oxidation of kenomagnetite to hematite is followed by depletion of Mg, Co and Ni; and enrichment of As and REE; (ii) recrystallization of granoblastic hematite is commonly accompanied by enrichment in immobile elements (Ti, Al, V, Cr and Mo) due to removing of mobile elements (Mg, Mn, and As); (iii) late-stage specular hematite has very low concentrations of most trace elements relative to paragenetically early-stage iron oxides, similar to previous analyses on shear vein-hosted specular hematite from another iron deposits (Hensler et al., 2015; Oliveira et al., 2015).

2. The iron enrichment in the high-grade orebodies of the PLD deposit is related to the same anatectic event of the Borrachudos-hosted pegmatites; and could be explained by the following processes (Fig. 23): (i) Influx of anatectic fluids during the metamorphic event of the Brasiliano orogen and formation of the high-grade orebodies through silica leaching; (ii) Hematite crystallization in high-grade orebodies during silica and trace elements leaching and the formation of Vp1 veins; (iii) A second-stage of magnetite crystallization (martite-II) during the the lowering of the pressure and the formation of the Vp2 veins.

According to the whole rock geochemical analyses, itabirites from Morro Escuro ridge, Guanhães and Dores de Guanhães prospects show evidences of a shallow marine depositional environment and secondary hydrothermal alteration; while the itabirite and HGI orebodies from PLD show a different hydrothermal alteration evolution and depositional environment.

Acknowledgments

This paper contains results of the PhD thesis of the first author at the Universidade Federal de Minas Gerais-UFMG, Brazil, who received a scholarship from Coordenação de Aperfeiçoamento de Pessoal de Nível Superior — CAPES. The main research funds were provided by FAPEMIG (grant APQ-0117815), and a project with joint resources from the Brazil's National Council of Technological and Scientific Development — CNPq and Vale.

References

AngloAmerican, 2014. Anglo American delivers first ore on ship from Minas Rio. http://www.angloamerican.com/media/press-releases/2014/27-10-2014. (accessed oct-2017).

Alkmim, F.F., Marshak, S., Pedrosa-Soares, A.C., Peres, G.G., Cruz, S.C.P., Whittington, A., 2006. Kinematic evolution of the Araçuaí-West Congo Orogen in Brazil and Africa: nutcracker tectonics during the neoproterozoic assembly of Gondwana. Precambrian Res., 149, 43-64.

Allan, M.M., Yardley, B.W.D., Forbes, L.J., Shmulovich, K.I., Banks, D.A., Shepherd, T.J., 2005. Validation of LA-ICP-MS fluid inclusion analysis with synthetic fluid inclusions. Am Mineral. 90, 1767-1775.

Almeida-Abreu, P.A., Renger, F.E., 2002. Serra do Espinhaço Meridional: Um Orógeno de Colisão do Mesoproterozóico, Revista Brasileira de Geociências; 32(1), 1-14.

Almeida, F.F.M. (1977). O Cráton do São Francisco. Revista Brasileira de Geociências, 7, 349-364.

Almeida, F.F.M., Brito Neves, B.B., Carneiro, C.D.R., 2000. The origin and evolution of the South American Platform. Earth-Science Rev. 50, 77-111.

Anderson, M.R., Rankin, A.H., and Spiro, B., 1992, Fluid mixing in the gen- eration of mesothermal gold mineralisation in the Transvaal Sequence, Transvaal, South Africa. European Journal of Mineralogy. 4, 933–948.

Barrote, V.R., 2016. A sequência portadora de formações ferríferas de Guanhães, Minas Gerais, Brasil. Dissertação (Mestrado). Belo Horizonte. Instituto de Geociências da UFMG, p.103.

Barbosa, J.S.F. and Sabate, P., 2004. Archean and Paleoproterozoic crust of the São Francisco Craton, Bahia Brazil: geodynamic features. Precamb. Res. 133, 1–27.

Bau M., Alexander, B., 2009. Distribution of high field strength elements (Y, Zr, REE, Hf, Ta, Th, U) in adjacent magnetite and chert bands and in reference standards FeR-3 and FeR-4 from the Temagami iron-formation, Canada, and the redox level of the Neoarchean ocean. Precambrian Research. 174, 337-346.

Bau, M., 1996. Controls on the fractionation of isovalent trace elements in magmatic and aqueous systems: evidence from Y/Ho, Zr/Hf, and lanthanide tetrad effect. Contrib. Mineral. Petrol. 123, 323–333.

Bau, M., Dulski, P., 1996. Distribution of yttrium and rare-earth elements in the Penge and Kuruman Iron-Formations, Transvaal Supergroup, South Africa. Precambrian Res. 79, 37-55.

Beukes, N.J., Gutzmer, J., 2008. Origin and paleoenvironmental significance of major iron formations at the Archean–Paleoproterozoic boundary. Rev. Econ. Geol. 15, 5–47.

Bilal E., Marciano V.R.P.R.O., Fuzikawa K., Correia Neves J.M., Giret, A., 1995. Datação de monazitas do Distrito Pegmatítico de Santa Maria de Itabira, MG. In: SBG/ Núcleo MG, Simp. Geol. Minas Gerais, 8, Diamantina, Boletim, 13:46-47.

Bodnar, R.J., Vityk, M.O., 1994. Interpretation of microthermometric data for H_2O-NaCl fluid inclusions. In: de Vivo, B., Frezzotti, M.L. (Eds.), Fluid Inclusions in Minerals: Methods and Applications. Short Course IMA, p.117–130.

Bowers, T.S., Helgeson, H.C., 1983. Calculation of the thermodynamic and geochemical consequences of nonideal mixing in the system H2O–CO2–NaCl on phase relations in geological systems: equation of state for H2O–CO2–NaCl fluids at high pressures and temperatures. Geochim. Cosmochim. Acta. 47, 1247-1275.

Brown, P.E., Hagemann, S.G., 1995. MacFlinCor and its application to fluids in Archaean lode-gold deposits. Geochim. Cosmochim. Acta 59, 3943–3952.

Braga, F.C.S., Rosiere, C.A., Queiroga, G.N., Rolim, V.K., Santos, J.O.S., McNaughton, N.J., 2015. The Statherian itabirite-bearing sequence from the Morro Escuro Ridge, Santa Maria de Itabira, Minas Gerais, Brazil. J. S. Am. Earth Sci. 58, 33-53.

Campos, C.P., Medeiros, S.R., Mendes, J.C., Pedrosa-Soares, A.C., Dussin, I., Ludka, I.P., Dantas, E.L., 2016, Cambro-Ordovician Magmatism in the Araçuaí Belt (SE Brazil): snapshots from a post-collisional event. Journal of South American Earth Sciences, v. 68, p. 248-268.

Carvalho, R.P., Rosiere, C.A., Rolim, V.K., Lana, C.C., Santos, J.O.S., 2014. A sequência orosiriana-estateriana e geometria transpressiva na região de Santa Maria de Itabira-MG. Rev. Inst. Geociências-USP 14 (2), 101-120.

Centaurus Metals Ltd., 2008. Initial JORC Resource for Liberdade Project, Perth: ASX Release.

Centaurus Metals Ltd., 2014. September 2014 Quarterly Activities Report, Perth: ASX Release.

Chemale Jr., F., Quade H., Schmus W.R.V, 1998. Petrography, geoquemistry and geochronology of the Borrachudos and Santa Bárbara metagranites, Quadrilátero Ferrífero, Brazil. Zbl. Geol. Palaont, Stuttgart, I, 3-6, 739-750.

Chemale Jr., F., Dussin, I.A., Alkmim, F.F., Martins, M.S., Queiroga, G., Armstrong, R., Santos, M.N., 2012. Unravelling a Proterozoic basin history through detrital zircon geochronology: the case of the Espinhaço Supergroup, Minas Gerais, Brazil. Gondwana Research, 22(1), 200-206.

Cordani, U.G., Fraga, L.M., Reis, N., Tassinari, C.C.G., Brito-Neves, B.B., 2010. On the origin and tectonic significance of the intra-plate events of Grenvillian-type age in South America: a discussion. Journal of South American Earth Sciences 29, 143–159.

Correia Neves, J.M., Pedrosa Soares, A.C., Marciano, V.R.P.da R.O., 1986. A província pegmatítica oriental do Brasil à luz dos conhecimentos atuais. Rev. Bras. Geoc. 16 (1), 106-118.

Diamond, L.W., 1990, Fluid inclusion evidence for P-V-T-X evolution of hydrothermal solutions in late-Alpine gold-quartz veins at Brusson, Val d'Ayas, northwest Italian Alps. American Journal of Science. 290, 912–958.

Dorr, J.V.N. and Barbosa, A.L.M., 1963. Geology and ore deposits of the Itabira District Minas Gerais, Brazil: U. S. Geological Survey Professional Paper 341-C, p110.

Dorr, J.V.N., 1969. Physiographic, stratigraphic and structural development of the Quadrilatero Ferrifero, Minas Gerais, Brazil. United States Geological Survey. Professional Paper, 110-641.

Dossin, I.A., Dossin, T.M., Charvet, J., Cocherie, A., Rossi, P., 1993. Single-zircon dating by step-wise Pb-evaporation of Middle Proterozoic Magmatismo in the Espinhaço Range, Southeastern São Francisco Craton (Minas Gerais, Brazil). In: Simpósio do Craton do São Francisco, 2, Salvador, Anais, p39-42.

Dussin, T.M., 1994. The Borrachudos Suite, Mezoproterozoic A-type Granitic Magmatism in the São Francisco Craton (SE Brazil). In: Associacions vulcano- plutoniques de l'Espinhaço Meridional (SE - Brésil). Université d'Orleans, Orléans. PhD Thesis.

Dussin, I.A., Dussin, T.M., 1995. Supergrupo Espinhaço: modelo de evolução geodinâmica. Geonomos, 3(1), 19-26.

Dussin, T. M., Duarte, P., Dussin, I.A., 2000. Registro da tectônica Brasiliana na região de Guanhães (SE, Brasil): Deformação e metamorfismo das rochas de idade pós-Transamazônicas. Geonomos, 8(2), 55-59.

Fernandes M. L. S., Marciano V. R. P. R., Oliveira R. C., Correia Neves J. M., Dilascio M. V., 1994. Granitos Borrachudos: um exemplo de granitogênese anorogênica na porção central do estado de Minas Gerais. Belo Horizonte. Geonomos, 2,2. 23-29.

Fernandes, M.L.S., 2001. O Granito Borrachudos entre Guanhães e Dores de Guanhães (Plutonito Morro do Urubu): Gênese e Evolução. PhD thesis. Departamento de Geologia, Universidade Federal do Rio do Janeiro, p. 187.

Figueiredo e Silva, R.C., Hagemann, S.G., Lobato, L.M., Rosière, C.A., Banks, D.A., Davidson, G.J., Vennemann, T.W., Hergt, J.M., 2013. Hydrothermal fluid processes and evolu- tion of the giant Serra Norte jaspilite-hosted iron ore deposits, Carajás Mineral Province, Brazil. Econ. Geol. 108, 739-779.

Goldstein, R.H., Reynolds, T.J., 1994. Systematics of fluid inclusions in diagenetic minerals. SEPM Short Course 31. The Mineralogical Association of Canada, Tulsa, p199.

Grossi-Sad J.H., Chiod Filho C., Santos J.F., Magalhães J.M.M., Carelos P.M., 1990a. Duas Suítes Graníticas do Bordo Sudeste do Cráton Sanfrasciscano, em Minas Gerais: Petroquímica e Potencial Metalogenético. SBG, Congr. Bras. de Geol., 36, Natal, Anais, 4: 1836-1848.

Grossi-Sad, J.H., Chiodi Filho, C., Santos, J.F., Magalhães, J.M.M., Carelos, P.M., 1990b. Geoquímica e origem da formação ferrífera do Grupo Guanhães, Distrito de Guanhães, MG, Brasil. SBG, Congr. Bras. de Geol., 36, Natal, Anais, 3: 1241-1253.

Grossi-Sad, J.H., Mourão, M.A.A., Guimarães, M.L.V., Knauer, L.G., 1997. Geologia da Folha Conceição do Mato Dentro. In: Grossi-Sad, J.H., Lobato, L.M., Pedrosa- Soares, A.C., Soares-Filho, B.S. (Eds.), Projeto espinhaço Em CD-ROM (textos, mapas e anexos). COMIG e Companhia Mineradora de Minas Gerais, Belo Horizonte, pp. 2533-2693.

Guadagnin, F., Chemale Jr., F., Magalhães, A.J.C., Santana, A., Dussin, I., Takehara, L., 2015. Age constraints on crystal-tuff from the Espinhaço Supergroup — Insight into the Paleoproterozoic to Mesoproterozoic intracratonic basin cycles of the Congo–São Francisco Craton. Gondwana Research, 27, 363–376.

Guillong M.M., Maier D.L., Allan M.M., Heinrich C.A., 2008. SILLS: a MATLAB based program for the reduction of laser ablation ICPMS data of homogeneous materials and inclusions. Sylvester P (ed) Laser Ablation ICPMS in the Earth Sciences. Current Practices and Outstanding Issues, 328-333.

Hagemann, S.G., Angerer, T., Duuring, P., Rosière, C.A., Figueiredo e Silva, R.C., Lobato, L.M., Hensler, A.S., Walde, D.H.G., 2016. BIF-hosted iron mineral system: A review. Ore Geol. Rev. 76, 317–359.

Hensler, A.S., Hagemann, S.G., Rosière, C.A., Angerer,T., Gilbert, S., 2015. Hydrothermal and

metamorphic fluid-rock interaction associated with hypogene “hard” iron ore mineralisation in the Quadrilátero Ferrífero, Brazil: Implications from in-situ laser ablation ICP-MS iron oxide chemistry. Ore Geology Reviews. 69, 325-351.

Jordt-Evangelista, H., Lana, C., Delgado, C.E.R, Viana, D.J., 2016, Age of the emerald mineralization from the Itabira Nova Era District, Minas Gerais, Brazil, based on LAICPMS geochronology of cogenetic titanite. Brazilian Journal of Geology, 46(3), 427-437.

Klein, C., 2005. Some Precambrian banded iron-formations (BIFs) from around the world: their age, geologic setting, mineralogy, metamorphism, geochemistry, and origin. Am. Mineral. 90, 1473–1499.

Knauer, L.G., 1990. Evolução geológica do Precambriano da porção centro;leste da Serra do Espinhaço Meridional e metalogênese associada. Dissertação (Mestrado), Campinas, UNICAMP, p.298.

Marciano, V.R.P.R.O, Svisero, D.P, Correia-Neves, J.M., 1993, Dados geocronológicos de pegmatitos da borda oriental do Craton do São Francisco. Anais do Simp. sobre o Craton do São Francisco: Sua evolução tectonica e metalogenética. Salvador, SBG-Ba, SE/SGM, 362-365.

Marciano, V.R.P.R.O., 1995. O distrito pegmatítico de Santa Maria de Itabira, MG. Mineralogia, geoquímica e zoneografia. PhD Thesis. Inst. Geoc. Univ. São Paulo, p216.

Martins-Neto, M.A., 2000. Tectonics and sedimentation in a paleomesoproterozoic rift-sag basin (Espinhaço basin, southeastern Brazil). Precambrian Res. 103, 147-173.

Martins-Neto, M.A., and Hercos, C.M., 2002. Sedimentation and tectonic setting of Early Neoproterozoic glacial deposits in southeastern Brazil. International Association of Sedimentologists, Special Publication, 33: 383-403.

McLennan, S.M., 1989. Rare earth elements in sedimentary rocks: influence of provenance and sedimentary processes. In: Lipin, B.R., McKay, G.A. (Eds.), Geochemistry and Mineralogy of Rare Earth Elements, Reviews in Mineralogy. 21, 169-200.

Melo, M.G., Lana, C., Stevens, G., Pedrosa_Soares, A.C., Gerdes, A.A., Leonardo, A., Nalini, H.A., Alkmim, F.F., 2017, Assessing the isotopic evolution of S-type granites of the Carlos Chagas Batholith, SE Brazil: Clues from U?Pb, Hf isotopes, Ti geothermometry and trace element composition of zircon. Lithos, 284-285, 730-750.

Morteani, G., Preinfalk, C., Horn, A.H., 2000. Classification and mineralisation potential of the pegmatites of the Eastern Brazilian Pegmatite Province. Mineral. Deposita, 35, 638-655.

Müller G., Hõhndorf A., Lauenstein H.J., Lenz H., 1986a. Petrological and Geochemical data on a high-metamorphic Archean BIF - bearing rock sequence near Guanhães, Minas Gerais, Brazil. Geol. Jb., 3-20.

Müller, G., Schuster, A.K., Hoefs, J., 1986b. The metamorphic grade of banded iron formations: Oxygen isotope and petrological constraints: Fortschritte der Mineralogie, 64, 163-185.

Noce, C.M., Pedrosa-Soares, A.C., Silva, L.C., Armstrong, R., Piuzana, D., 2007. Evolution of polycyclic basement complexes in the Araçuai Orogen, based on U–Pb SHRIMP data: Implications for Brazil–Africa links in Paleoproterozoic time, Precambrian Res., 159, 60-78.

Oliveira, L.A.R., Rosière, C.A., Rios, F.J., Andrade, S., Moraes, R., 2015. Chemical fingerprint of iron oxides related to iron enrichment of banded iron formation from the Cauê Formation - Esperança Deposit, Quadrilátero Ferrífero, Brazil: a laser ablation ICP-MS study. Revista Brasileira

de Geociências, v. 45, p. 193-216.

Oliveira, L.A.R., Rios, F.J., Rosière, C.A., Wälle, M., Ortelli, M., Kouzmanov, K., 2017. Nature and evolution of fluids associated with specularite-bearing Fe and Au-PGE (Jacutinga) mineralization during the Brasiliano orogeny in the eastern São Francisco Craton, Minas Gerais, Brazil. Ore Geology Reviews 86, 130–153.

Pecoits, E., 2010. Ediacaran Iron Formations and Carbonates of Uruguay: Palae-oceanographic, Palaeoclimatic and Palaeobiologic Implications. PhD thesis. University of Alberta, p.230.

Pedrosa-Soares, A.C., Cordani, U., Nutman, A., 2000. Constraining the age of Neoproterozoic glaciation in eastern Brazil: First U-Pb SHRIMP data from detrital zircons. Rev. Bras. de Geociênc., 30: 58-61.

Pedrosa-Soares, A.C., Noce, C.M., Wiedemann, C.M., Pinto, C.P., 2001. The Araçuai-West Congo orogen in Brazil: An overview of a confined orogen formed during Gondwanland assembly. Precamb. Res., 110, 307–323.

Pedrosa-Soares, A.C., Noce, C M., Alkmim, F.F., Silva, L.C., Babinski, M., Cordani, U., Castañeda, C., 2007. Orógeno Araçuaí: síntese do conhecimento 30 anos após Almeida 1977. Geonomos, 15(1), 1-16.

Pedrosa-Soares, A.C., Campos, C.P., Noce, C., Silva, L.C., Novo, T., Roncato, J., Medeiros, S., Castaneda, C., Queiroga, G., Dantas, E., Dussin, I.A., Alkmim, FF. 2011. Late Neoproterozoic–Cambrian granitic magmatism in the Araçuai orogen (Brazil), the Eastern Brazilian Pegmatite Province and related mineral resources. Geological Society, London, Special Publications, 350, 25–51.

Pflug, R., 1965. A geologia da parte meridional da Serra do Espinhaço e zonas adjacentes, Minas Gerais. DNPM/DGM, Bol. 226., Rio de Janeiro, p.1-51.

Preinfalk, C., Kostitsyn, Y., Morteani, G., 2002. The pegmatites of the Nova Era - Itabira - Ferros pegmatite district and the emerald mineralisation of Capoeirana and Belmont (Minas Gerias, Brazil): geochemistry and Rb-Sr dating. Jour. South Am Earth Scienc., 14, 867-887.

Purtov, V.K., Kotelnikova, A.L., 1993. Solubility of titanium in chloride and fluoride hydrothermal solutions. Int. Geol. Rev. 35, 279-287.

Roedder, E., 1984. Fluid inclusions. Rev. Mineral. 12. Mineralogical Society of America, p. 646.

Rolim, V.K., 2016. As Formações Ferríferas da Região de Conceição do Mato Dentro – MG: Posicionamento Estratigráfico, Evolução Tectônica, Características Geoquímicas e Gênese dos Minérios (Ph.D. thesis). Universidade Federal de Minas Gerais, Brazil, 242pp.

Rolim, V.K., Rosière, C.A., 2011. The Conceição do Mato Dentro Iron Formation Province in southeastern Brazil. In: Let's Talk Ore Deposits: Proceedings of the 11th Biennial SGA Meeting, Antofagasta, Chile. https://sga.conference-services.net/resources/1054/2590/pdf/SGA2011_0237.pdf. (accessed 24.11.2016).

Rolim, V.K., Rosière, C.A., Santos, J.O.S., McNaughton, N.J., 2016. The Orosirian-Statherian banded iron formation-bearing sequences of the southern border of the Espinhaço Range, Southeast Brazil. J. S. Am. Earth Sci. 65, 43-66.

Rosière, C.A., Spier, C.A., Rios, F.J., Suckau, V.E., 2008. The itabirites of the quadrilatero ferrifero and related high-grade iron ore deposits: an overview. Rev. Econ. Geol. 15, 223-254.

Silva, L.C., Armstrong, R., Noce, C.M., Carneiro, M.A., Pimentel, M.M., Pedrosa- Soares, A.C., Leite, C.A., Vieira, V.S., Silva, M.A., Paes, V.J.C., Cardoso-Filho, J.M., 2002. Reavaliação da evolução geológica em terrenos pre cambrianos brasieiros com base em novos dados U-Pb SHRIMP, parteII: Orógeno Araçuaí, Cinturão Mineiro e Cráton São Francisco Meridional. Rev. Bras. Geociênc. 32, 513-528.

Silveira, E.M., Söderlund, U., Oliveira, E.P., Ernst, R.E., Menezes Leal, A.B., 2013. First precise U-Pb baddeleyite ages of 1500 Ma mafic dykes from the São Francisco Craton, Brazil, and tectonic implications. Lithos 174, 144–156.

Taylor, S.R. and McLennan, S.M., 1985. The Continental Crust: Its Composition and Evolution. Blackwell, London.

Thorne, W.S., Hagemann, S.G., Sepe, D., Dalstra, H.J., Banks, D.A., 2014. Structural control, hydrothermal alteration zonation, and fluid chemistry of the concealed, high-grade 4EE iron orebody at the Paraburdoo 4E Deposit, Hamersley Province, Western Australia. Econ. Geol. 109, 1529-1562.

Uhlein, A., Trompette, R.R., Egydio-Silva, M., 1998. Proterozoic rifting and closure, SE border of the São Francisco Craton, Brazil. J. South Am. Earth Sci. 11, 191-203.

Figure 1. Geological setting of the Southern Espinhaço Range with the location of the studied areas (red box and two red circles). The western limit of the Eastern Pegmatite Province is also shown with a dashed line. PLD (Piçarrão-Liberdade deposit), ME (Morro Escuro ridge), GNH (Guanhães prospect), DGN (Dores de Guanhães prospect), SFC (São Francisco Craton), AFB (Araçuaí fold belt). Adapted from Grossi-Sad et al., 1997.

Figure 2. Geology of the Piçarrão-Liberdade iron and alexandrite-beryl pegmatite deposits, as well as the Morro Escuro ridge area. Adapted from Carvalho et al. (2014).

Figure 3. Photographs of hand specimens of the itabirite and ores from the Piçarrão-Liberdade deposit. A. s34a – non-mineralized itabirite with hematite and quartz microbands, schistose fabric and quartz-martite vein. B. s36b - high-grade iron ore with granoblastic hematite. C. s34b - high-grade iron ore with kenomagnetite-I and granoblastic hematite in contact with itabirite. D. ss1 – foliated, high-grade iron ore with tabular hematite. Sn: foliation. Vp2 veins classification: see section 4.1.2.

Figure 4. Photomicrographs (reflected, polarized light) showing itabirite mineralogy, in samples. A. s34a - non-mineralized itabirite with schistose fabric, showing martite-I with relic kenomagnetite (in circular blow up), lamelar hematite and quartz microbands; martite grains are overprinted by lamelar hematite. B. s36b - high-grade iron ore with granoblastic hematite. C. s34b - high-grade iron ore with kenomagnetite-I relicts in martite-I, martite grains are overprinted by granoblastic hematite. D. ss1 - high-grade iron ore with granoblastic hematite overprinted by tabular hematite. The tabular hematite shows a preferred orientation E. s35 - quartz-martite-II vein with kenomagnetite-II replaced by martite-II. F. ss2 – kenomagnetite-I overprinted by granoblastic hematite. Martitization of kenomagnetite is along grain boundary in contact with the granoblastic hematite. GbHem: granoblastic hematite; KMag: kenomagnetite; LmHem: lamelar hematite; Mt: martite; Qtz: quartz; TbHem: tabular hematite.

Figure 5. Iron oxide paragenetic sequence of itabirite-hosted iron ore at Piçarrão-Liberdade deposit, Morro Escuro ridge, Guanhães and Dores de Guanhães prospects. The classification of the quartz crystals used in the fluid inclusions studies is also shown. Qtz: quartz.

Figure 6. Schematic diagram illustrating the different vein types (Vp1, Vp2, Vpe, Vms, Vmi). A. Piçarrão-Liberdade deposit B. Morro Escuro ridge. Sn: foliation.

Figure 7. Results of whole-rock geochemical analyses of itabirite-hosted high-grade iron rock. Distribution pattern of the REE + Y values of the hematite and itabirites normalized to the values of PAAS (McLennan, 1989) in relation to itabirite for each deposit. PLD (Piçarrão-Liberdade deposit); ME (Morro Escuro ridge); GNH (Guanhães and Dores de Guanhães prospects). HGI: high-grade iron.

Figure 8. Ce/Ce*(SN) vs.Y/Ho diagram showing a comparison of trace element data derived from whole-rock geochemical analyses of itabirite-hosted high-grade iron rock (Pecoits, 2010). Symbols: Black (Piçarrão-Liberdade); gray (Morro Escuro); white (Guanhães-Dores de Guanhães). HGI: high-grade iron.

Figure 9. Discrimination diagram, derived from whole-rock geochemical analyses, of Ce/Ce*(SN) vs. Pr/Pr*(SN) for La and Ce anomalies (Bau and Dulsky, 1996). It shows a variation from positive Ce anomaly in the itabirites to negative Ce anomaly in the HGIs. PLD (Piçarrão-Liberdade), ME (Morro Escuro), GNH (Guanhães-Dores de Guanhães). HGI: high-grade iron.

Figure 10. Box-and-whisker plots of minor and trace elements in ppm from mineral chemistry LA-ICP-MS data. The results are grouped by iron oxide mineral for the Piçarrão-Liberdade deposit.

The upper and lower margins of the box represent the upper and lower 50 percentile of the data. The whiskers represent the upper and lower threshold values (95 percentile of the data). Median values are shown as solid black lines and mean values as solid black circles. See Fig. 4 for oxide paragenetic sequence. HGI: high-grade iron.

Figure 11. Rare earth element PAAS-normalized (McLennan, 1989) spider plot of iron oxide mineral chemistry data from A. Piçarrão-Liberdade deposit; B. Morro Escuro ridge, and C. Dores de Guanhães and Guanhães prospects. HGI: high-grade iron.

Figure 12. Box-and-whisker plots, derived from mineral chemistry LA-ICP-MS data, of minor and trace elements in ppm grouped by iron oxide mineral for Morro Escuro ridge. The upper and lower margins of the box represent the upper and lower 50 percentile of the data. The whiskers represent the upper and lower threshold values (95 percentile of the data). Median values are shown as solid black lines and mean values as solid black circles. See Fig. 4 for oxide paragenetic sequence. HGI: high-grade iron.

Figure 13. Box-and-whisker plots of minor and trace elements in ppm from mineral chemistry LA-ICP-MS data. The results are grouped by iron oxide mineral for Dores de Guanhães and Guanhães prospects. The upper and lower margins of the box represent the upper and lower 50 percentile of the data. The whiskers represent the upper and lower threshold values (95 percentile of the data). Median values are shown as solid black lines and mean values as solid black circles. See Fig. 4 for oxide paragenetic sequence. HGI: high-grade iron.

Figure 14. Fluid inclusion samples, and fluid inclusion maps showing analyzed fluid inclusion assemblages hosted by Vp1 veins from the Piçarrão-Liberdade iron deposit. A. sample s31 - thin section surface of Vp1 quartz (Qtz1) vein with border of granoblastic hematite (Hem). B. Photomicrograph of Qtz1 showing selected fluid inclusion areas for microthermometric analyses. C. Insets displaying fluid inclusion maps with FI assemblage number. D. Photomicrograph of Qtz1 showing pseudosecondary trail selected for microthermometric analyses. E. Photomicrograph of the selected trail displaying fluid inclusion map with assemblage number. F. Type 2 inclusion trapped in Qtz1 from Area A. FIA: Fluid Inclusion Assemblage.

Figure 15. Fluid inclusion samples and fluid inclusion maps showing analyzed fluid inclusion assemblages hosted by Vp2 veins from the Piçarrão-Liberdade iron deposit. A. sample s01 - quartz-martite-II vein (Vp2) and location of double-polished thin section used for microthermometry. B. Photomicrograph of quartz (Qtz2) with pseudosecondary and secondary FI trails. C. Inset A that shows a map of fluid inclusions analyzed, displaying fluid inclusion sample map with assemblage number. D. sample s03 - photomicrograph of Qtz2 and martite-II with secondary fluid inclusion trail and one area where pseudosecondary fluid inclusion are observed (see inset B). E. Inset B displaying pseudosecondary fluid inclusions and assemblage number. F. Type 1 fluid inclusion trapped in Qtz2 from FIA01. FIA: Fluid Inclusion Assemblage.

Figure 16. Fluid inclusion samples, and fluid inclusion maps showing analyzed fluid inclusion assemblages hosted by Vpe veins from the Piçarrão-Liberdade iron deposit. A. sample s47 - diamond drill core (31m depth) displaying Vpe vein and sampling location. B. Photomicrograph of quartz (Qtz3) showing map of fluid inclusions. C and D. Insets displaying fluid inclusion sample map with assemblage number. FIA – Fluid Inclusion Assemblage. Kf: K-feldspar.

Figure 17. Fluid inclusion samples, and fluid inclusion maps showing analyzed fluid inclusion assemblages hosted by Vmi and Vms veins from Morro Escuro ridge as well as beryl samples from Ponte da Raiz pegmatite. A. sample s07 displaying Vmi vein and sampling location. B. Photomicrograph of quartz (Qtz1a) from Vmi showing mapping of fluid inclusions (hematite - Hem). C. Inset displaying fluid inclusion sample map with assemblage number. D. sample s08 - photomicrograph of Qtz1a from Vms showing mapping of fluid inclusions. E. Inset displaying fluid inclusion sample map with assemblage number. F. Photomicrograph of beryl (sample Be01) showing mapping of fluid inclusions types. FIA – Fluid Inclusion Assemblage.

Figure 18. Salinity (eq. wt. % NaCl) versus homogenization temperature (°C) data for fluid inclusion assemblages trapped in quartz (Vp1, Vp2, Vpe, Vmi and Vms veins) and beryl (Vb). Dashed lines represent fluid inclusion assemblages.

Figure 19. Diagrams showing metal concentrations (ppm) obtained from LA-ICP-MS analyses on individual fluid inclusions. The shaded box is the 25^{th} and 75^{th} percentiles, with the median value (horizontal lines) and mean value (black circle). The lower and upper horizontal lines are the 5^{th} and 95^{th} percentiles; outliers are individual points.

Figure 20. Bivariate and ternary plots of LA-ICP-MS element ratios (alkali and alkaline earths and transition metals) of individual fluid inclusions trapped in quartz from Vp1, Vp2, and Vpe veins at Piçarrão-Liberdade deposit.

Figure 21. Bivariate and ternary plots of LA-ICP-MS element ratios (alkali and alkaline earths and transition metals) of individual fluid inclusions trapped in quartz from Vmi and Vms veins at Moro Escuro ridge.

Figure 22. Binary plot illustrating Eu anomalies and the Y/Ho ratios derived from mineral LA-ICP-MS analyses. The Eu anomaly is calculated $Eu/Eu_{SN} = (Eu_{PAAS}/(0.5 \times Sm_{PAAS} + 0.5 \times Gd_{PAAS})$. The shadowed areas define the behavior of Y/Ho ratios of modern seawater and the chondritic-like CHARAC field (Bau, 1996). (HGI: high-grade iron; PLD – Piçarrão-Liberdade; ME Morro Escuro; DGN Dores de Guanhães).

Figure 23. Schematic illustration showing the interaction of high salinity and temperature fluids during the leaching of gangue minerals (silica), and the formation of high-grade iron orebodies and Vp1 veins. The Vp2 veins present martite enriched in trace elements, and lower salinity and temperature fluids trapped in the Qtz2. Kmag: kenomagnetite; LmHem: lamelar hematite; Mt: martite. GbHem:granoblastic hematite; Qtz: quartz.

Table 1. Vein types classified at the studied areas.

Table 2. Analyzed fluid inclusion types. PLD: Piçarrão-Liberdade deposit; ME: Morro Escuro rigde.

Table 3. Microthermometric results of pseudosecondary fluid inclusion assemblages. PLD: Piçarrão-Liberdade deposit; ME: Morro Escuro rigde.

Table 4. Summary of LA-ICP-MS analysis on fluid inclusion. Element/Na weight ratios and element concentrations in ppm, calculated using the salinity of the fluid inclusions. RSD (relative standard deviation). sd (standard deviation). bdl (below detection limit).

Appendix A. Chemical composition of the itabirite and high-grade samples. PLD: Piçarrão-Liberdade deposit; ME: Morro Escuro ridge; GNH: Guanhães prospect; DGN: Dores de Guanhães prospect; HGI: high-grade iron; LOI: loss on ignition; LOD: limit of detection; bdl: below detection limit; sd: standard deviation.

Appendix B1. iron oxide compositions determined by LA-ICP-MS at Piçarrão-Liberdade deposit. HGI: High-grade iron bodies. sd: standard deviation.

Appendix B2. iron oxide compositions determined by LA-ICP-MS at Morro Escuro ridge. HGI: High-

grade iron bodies. sd: standard deviation.

Appendix B3. iron oxide compositions determined by LA-ICP-MS. GNH: Guanhães prospect. GDN: Dores de Guanhães prospect. HGI: High-grade iron bodies. sd: standard deviation.

Table 1.

Deposit/Area	Vein Type	Mineralogy	Host rock	Thickness	Geometry
Picarrão-Liberdade	Vp1	Quartz (Qtz1)	Quartz vein in high-grade Fe ore	centimetric	Lenticular
Picarrão-Liberdade	Vp2	Quartz (Qtz2)-martite-II	Coarse-grained vein hosted in itabirite	decimetric	Tabular-discordant
Picarrão-Liberdade	Vpe	Quartz (Qtz3)-K-feldspar-plagioclase	Pegmatite vein hosted in gneiss	centimetric	Tabular-discordant
Morro Escuro	Vmi	Quartz (Qtz1a)	Quartz vein hosted in itabirite	centimetric	Lenticular-concordant
Morro Escuro	Vms	Quartz (Qtz1a)	Quartz vein hosted in quartz schist	decimetric	Lenticular-concordant
Ponte da Raiz Pegmatite	Vb	Quartz-K-feldspar-beryl	Pegmatite	metric	Tabular-discordant

Table 2.

Deposit/Area	Samples	Vein Type	Mineral	Fluid inclusion type	Timing	Microthermometry	LA-ICP-MS
Picarrão-Liberdade	s31	Vp1	Quartz (Qtz1)	Type 1 – Aqueous	S		
				Type 2 - Aqueous-carbonic	PS	x	x
Picarrão-Liberdade	s01, s03	Vp2	Quartz (Qtz2)	Type 1 - Aqueous	PS	x	x
				Type 1 - Aqueous	S		
Picarrão-Liberdade	s47	Vpe	Quartz (Qtz3)	Type 1 - Aqueous	PS	x	x
				Type 1 - Aqueous	S		
Morro Escuro	s07	Vmi	Quartz (Qtz1a)	Type 1 – Aqueous	PS	x	
				Type 2 - Aqueous-carbonic	PS	x	x
Morro Escuro	s08	Vms	Quartz (Qtz1a)	Type 1 – Aqueous	PS	x	
				Type 2 - Aqueous-carbonic	PS	x	x
Ponte da Raiz	Be1	Vb	Beryl	Type 2a – Aqueous-carbonic	P	x	
				Type 2b – Aqueous-carbonic	PS	x	
				Type 2c - Aqueous-carbonic	PS	x	

Abbreviations: PS = pseudosecondary, S = secondary

Table 3.

Vein/ host mineral	Deposit / Area	Phase(s)	Assem-blage	n	TmIce (°C)	Tclath (°C)	$TmCO_2$ (°C)	$ThCO_2$ (°C)	XCO_2	ThTot (°C)	Tm(hal) (°C)	Salinity (wt. % NaCl equiv.)
Vp1	PLD	L-L-V-S	8	1		9	-56.7	30.9	0.086	315	86.5	27.6
Quartz (Qtz1)	PLD	L-L-V-S	9	3		8.5	-56.7	27.5 ± 3	0.215	310 ± 5	87	27.6
	PLD	L-L-V-S	10	2		7.5 ± 0.5	-56.7	31.2 ±0.1	0.086	305 ± 10	87	27.6
	PLD	L-L-V-S	11	5		9.1 ± 0.5	-57.9	28.5 ± 3.3	0.213	315 ± 15	83 ± 10	27.5
	PLD	L-L-V-S	12	7		9.0 ± 0.8	-56.6	25 ± 1.5	0.305	329 ± 15	70 ± 10	26.5 ± 1
	PLD	L-L-V-S	13	2		8.6	-56.6	31.5	0.086	373	70 ± 10	27.2 ± 1
	PLD	L-L-V-S	14	5		8.5 ± 0.8	-56.6	31 ± 1.5	0.086	315 ± 15	72 ± 10	27.2
	PLD	L-L-V-S	15	5		8.2 ± 0.5	-56.6	27.6 ± 5.4	0.215	323 ± 15	80 ± 10	27.4
	PLD	L-L-V-S	16	5		8.2 ± 0.7	-56.6	27.3 ± 6	0.215	270	83	27.5
Vp2	PLD	L-V	1	3	-0.9 ± 0.1					190 ± 5		1.5
Quartz (Qtz2)	PLD	L-V	2	3	-8.5 ± 0.5					244 ± 5		12.7 ± 1.5
	PLD	L-V	3	5	-3 ± 2.5					144 ± 20		4.96
	PLD	L-V	4	6	-8.5 ± 1.5					260 ± 5		12.7 ± 1
	PLD	L-V	5	2	-1.8 ± 1.2					160		3.06
	PLD	L-V	6	10	-1.6 ± 0.4					145 ± 5		2.74 ± 1.5
	PLD	L-V	7	8	-0.7 ± 0.1					152.7 ± 14.7		1.23
Vpe	PLD	L-V	17	6	-2.1 ± 1.6					156 ± 10		3.55
Quartz (Qtz3)	PLD	L-V	18	5	-2.4 ± 0.9					156 ± 10		4.03
	PLD	L-V	19	9	-6.1 ± 0.6					348 ± 55		9.34 ± 1
Vmi	ME	L-L-V-S	20	2		7.6 ± 2	-56.6	27.6 ± 2	0.287	290	51 ± 5	26.8
Quartz (Qtz1a)	ME	L-L-V-S	21	5		8.0 ± 3	-56.6	29.7 ± 3	0.027	340 ± 20	58 ± 5	26.9 ± 1
	ME	L-L-V-S	22	1		7.7	-56.6	32	0.128	310	35	26.6
	ME	L-L-V-S	23	1		8.2	-56.6	22.4	0.142	300	37	26.6
	ME	L-V	24	5	-1.8 ± 0.6					157 ± 15		4.55 ± 1

Table 3 (cont.).

Vms	ME	L-L-V-S	25	3		9.8 ± 2	-56.6	30	0.058	250	58 ± 4	26.9
Quartz (Qtz1a)	ME	L-V	26	2	-2.5 ± 0.3					140		4.18
	ME	L-L-V-S	27	5		9.3 ± 0.5	-56.6	31 ± 1.5	0.128	230 ± 10	58.8 ± 10	26.9
	ME	L-L-V	28	4		5.0 ± .5	-56.6	15.4	0.126	235		9
	ME	L-L-V	29	6		6.1 + 0.5	-56.6	25 ± 4	0.126	230 ± 10		7 ± 2
	ME	L-V	30	3	-11 ± 1					130		14.97
	ME	L-L-V	31	3		6.0 ± 0.3	-56.6	25	0.021	220		7
Vb	Ponte da Raiz	L-L-V-S	32	7		4.3 ± 0.9	-56.9	28.5 ± 2.6	0.285	320 ± 10	125 ± 20	28.7
Beryl	Ponte da Raiz	L-L-V-S	33	3		4.6 ± 1.2	-57.7	31.4 ± 0.6	0.128	315	135 ± 40	29.2
	Ponte da Raiz	L-L-V-S	34	4		9.2 ± 0.6	-56.6	31 ± 0.8	0.058	315	126 ± 15	28.7

Table 4.

	Vp1					Vp2					Vpe				
	ratio (mean)	RSD	ppm (mean)	sd	n	ratio (mean)	RSD	ppm (mean)	sd	n	ratio (mean)	RSD	ppm (mean)	sd	n
Na	1	0	44730	21202	36	1	0	7641	6054	73	1	0	6745	2352	33
K	.483	43	9731	9851	22	1.44	48	6060	6931	50	.676	47	3159	2026	28
Ca	.514	47	12136	9660	27	.438	48	2134	2217	58	.364	53	1479	1099	25
Mg	.108	66	1841	2813	17	.223	86	1066	1695	47	.224	81	1049	1107	26
Mn	.015	76	84	277	6	.025	164	30	83	20	.027	41	28	79	6
Fe	.332	81	2731	5296	11	.418	69	1852	2320	49	.215	72	759	827	22
Cu	.255	57	4770	4881	22	.086	85	226	294	45	.140	51	561	554	22
Zn	.105	64	2060	2191	23	.048	116	151	139	55	.146	71	876	665	33
Sr	.002	51	87	63	33	.002	75	14	19	59	.002	61	14	11	32
Ag	.001	84	11	23	11	.0003	126	.277	1.36	9	.0008	91	.84	2.05	8
Ba	.011	77	298	332	27	.004	79	14	22	46	.006	66	35	28	29
Pb	.02	66	462	508	24	.004	72	13	16	45	.008	72	29	40	19
Li	.049	55	537	1062	10	<LOD					.02	54	24	79	5

	Vmi					Vms				
	ratio (mean)	RSD	ppm (mean)	sd	n	ratio (mean)	RSD	ppm (mean)	sd	n
Na	1	0	27107	12492	27	1	0	26121	7525	36
K	2.17	47	45437	15231	27	1.91	25	43603	14465	35
Ca	.444	54	8215	4634	25	.440	38	9636	4717	33
Mg	.111	47	1979	1860	22	.293	78	4124	4871	24
Mn	.004	83	21	51	8	.002	86	13	32	10
Fe	.155	53	4039	4020	25	.057	63	1370	1110	33
Cu	.020	43	261	335	17	.021	47	386	338	27
Zn	.009	40	159	212	19	.018	62	458	287	36
Sr	.001	44	34	31	23	.001	51	38	22	34
Ag	.0002	83	1.57	3.8	8	.0002	128	.77	4.24	4
Ba	.003	56	24	51	10	.0008	55	13	15	23
Pb	.001	48	20	20	17	.003	61	98	74	35
Li	<LOD					.025	149	59	328	4

Appendix A.

Sample	LOD	ME2B	PB2A	GU1	LI3SUL	LI1	LI4SUL	L1S4E	LI7A	PB1A	ME2A	PB3A	PB4A	GB	DG2	GI3
Area/deposit		ME	ME	GNH	PLD	PLD	PLD	PLD	PLD	ME	ME	ME	ME	GNH	DGN	GNH
Rock type		Itabirite	Itabirite	Itabirite	Itabirite	Compact HGI	Banded HGI	Foliated HGI	Foliated HGI	Compact HGI	Compact HGI	Banded HGI	Foliated HGI	Compact HGI	Banded HGI	Foliated HGI
wt%	wt%															
SiO_2	0.01	42.02	45.52	44.86	45.71	1.3	0.82	0.22	3.93	0.23	0.8	19.66	0.21	0.29	0.31	0.53
Al_2O_3	0.01	0.26	0.14	0.17	0.23	0.79	0.47	0.39	0.31	0.44	0.52	0.51	1.29	0.5	1.24	0.17
Fe_2O_3 (Total)	0.01	56.07	55.1	53.54	52.94	98.78	96.1	99.67	95.31	96.3	96.89	77.84	99.18	95.63	97.98	97.85
MgO	0.01	0.02	0.02	0.07	0.01	0.1	0.19	0.04	0.03	3.55	0.04	0.03	0.03	3.81	0.03	0.02
CaO	0.01	bdl	bdl	bdl	bdl	bdl	bdl	bdl	bdl	0.03	bdl	bdl	bdl	0.13	bdl	bdl
Na_2O	0.01	bdl	bdl	bdl	bdl	bdl	bdl	bdl	bdl	bdl	bdl	bdl	bdl	bdl	bdl	0.01
K_2O	0.01	bdl	bdl	bdl	bdl	bdl	bdl	bdl	bdl	bdl	0.07	bdl	0.01	bdl	0.01	bdl
TiO_2	0.01	0.008	0.01	0.006	0.008	0.044	0.015	0.023	0.009	0.021	0.032	0.01	0.066	0.022	0.063	bdl
MnO	0.01	0.035	0.12	0.032	0.015	0.084	0.033	0.019	0.086	0.413	0.112	0.017	0.015	0.436	0.017	0.018
P_2O_5	0.01	0.03	0.03	0.01	bdl	0.05	0.17	0.02	bdl	0.06	0.24	0.13	0.11	0.03	0.09	0.01
Sum	0.01	98.48	100.9	98.67	100.6	100.7	98.49	100.4	99.32	98.62	98.76	100.3	100.9	98.34	100.7	100.7
LOI		0.06	0	0	1.69	0	0.71	0.05	0	0	0.1	2.11	0.04	0	0.95	2.1
FeO	0.1	0.9	1	1	1.6	12.8	6.3	1.2	4.2	6.5	9.5	0.9	0.8	20.7	1.8	2.2
Fe_2O_3	0.01	55.07	53.99	52.43	51.16	84.54	89.1	98.34	90.64	89.07	86.33	76.84	98.07	72.61	95.98	95.4
ppm	ppm															
La	0.05	2.53	1.21	1.77	2.25	0.81	11.6	2.7	0.53	4.18	1.64	1.57	4.29	1.11	5.33	0.51
Ce	0.05	8.02	2.94	3.1	15.2	3.01	15.3	46	1.83	3.31	3.21	2.42	8.29	1.28	10.4	0.78
Pr	0.01	0.59	0.4	0.37	0.34	0.17	3.1	0.5	0.08	0.79	0.32	0.26	1.1	0.16	1.3	0.05
Nd	0.05	2.25	2.66	1.6	1.24	0.63	10.9	2.2	0.3	2.59	1.41	0.89	4.58	0.55	5.6	0.19
Sm	0.01	0.45	1.17	0.35	0.2	0.15	1.98	0.53	0.11	0.44	0.27	0.17	1.05	0.12	1.41	0.04
Eu	0.005	0.138	0.348	0.13	0.052	0.062	0.373	0.179	0.041	0.182	0.114	0.063	0.351	0.044	0.354	0.038
Gd	0.01	0.49	1.4	0.34	0.36	0.33	1.49	0.71	0.43	0.33	0.31	0.19	1.64	0.1	1.69	0.11
Tb	0.01	0.08	0.23	0.06	0.07	0.07	0.21	0.13	0.09	0.06	0.05	0.03	0.37	0.01	0.33	0.02
Dy	0.01	0.47	1.11	0.38	0.45	0.44	1.04	0.81	0.57	0.3	0.32	0.21	2.93	0.08	2.21	0.14

Appendix A (cont.).

Ho	0.01	0.09	0.18	0.08	0.1	0.09	0.19	0.16	0.12	0.05	0.08	0.05	0.69	0.02	0.51	0.03
Er	0.01	0.25	0.48	0.23	0.34	0.32	0.47	0.51	0.35	0.15	0.23	0.18	2.32	0.05	1.64	0.11
Tm	0.005	0.03	0.067	0.042	0.054	0.064	0.067	0.08	0.055	0.021	0.033	0.035	0.374	0.012	0.273	0.016
Yb	0.01	0.15	0.4	0.28	0.35	0.47	0.44	0.51	0.36	0.15	0.19	0.26	2.28	0.09	1.79	0.11
Lu	0.002	0.016	0.06	0.039	0.042	0.066	0.067	0.08	0.052	0.026	0.027	0.043	0.303	0.013	0.241	0.018
Σ REE		15.554	12.655	8.771	21.048	6.682	47.227	55.099	4.918	12.579	8.204	6.371	30.568	3.639	33.078	2.162
As	0.1	3.2	2.3	0.5	bdl	1.9	1.7	0.2	3.4	5.6	3.8	1.5	1	2.1	1.4	21.8
Co	0.1	0.8	2.9	0.7	0.5	3.4	7.1	1.6	1.1	4.8	4.9	0.7	0.2	5.3	0.3	0.7
Cr	0.5	58	38.5	40.1	24.9	37.5	48.3	101	40.5	19.3	25	80.4	74.2	19.2	109	19.2
Cu	0.2	2.2	2.8	3.9	7.1	6.4	23.7	4.8	13.3	3.8	13.8	11	2.4	5.9	2.7	7.4
Hg (ppb)	10	bdl	bdl	bdl	40	210	270	130	60	bdl	bdl	20	bdl	bdl	bdl	350
Ni	0.5	4.4	4.1	3.6	2.7	7.9	7.2	4	5.2	7.9	10.7	2.4	2.1	7.6	2.7	4.1
Pb	0.5	41.3	0.9	0.6	0.6	4.6	8.5	2.5	1.7	4	2.1	9.2	5.2	2.8	4.1	1.3
Sr	0.2	2.1	7.6	1.3	0.9	0.9	6.8	1.3	0.9	2.4	21.7	1.4	24	1.3	19.8	1.1
Th	0.05	0.47	0.21	0.08	0.31	0.25	0.22	0.36	bdl	0.48	0.09	0.29	0.33	0.19	0.24	bdl
U	0.01	0.83	0.86	1.15	0.24	1.92	3.59	2.02	0.75	3.63	2.99	1.77	1.77	2.11	1.56	0.17
V	5	34	45	88	37	79	56	116	66	68	89	27	94	64	97	12
W	0.5	23.8	4.2	2	6.8	2.8	4	12.4	5.8	13.7	6.4	4.6	3.6	9.4	4	2.8
Y	0.5	2.4	6	2.4	4	2.7	4.9	5.5	4.8	1.5	2.8	2.4	22.5	0.6	16	1.2
Ce/Ce* (sn)		1.51	0.96	0.88	3.92	1.87	0.59	9.08	2.00	0.42	1.02	0.86	0.88	0.68	0.91	1.03
Eu/Eu* (sn)		1.44	1.34	1.77	0.89	1.19	1.05	1.38	0.73	2.14	1.95	1.75	1.14	2.17	1.05	2.63
Eu/Eu* (cn)		0.96	0.89	1.22	0.63	0.88	0.69	0.96	0.54	1.51	1.29	1.15	0.87	1.29	0.75	1.76
Pr/Yb(sn)		1.26	0.32	0.42	0.31	0.12	2.25	0.31	0.07	1.68	0.54	0.32	0.15	0.57	0.23	0.15

Ce/Ce*(sn)=Ce(sn)/(0.5Pr(sn) + 0.5La(sn)); Eu/Eu*(sn)=Eu(sn)/(0.67Sm(sn) + 0.33Tb(sn)); Eu/Eu*(cn) = Eu(cn)/(0.5Sm(cn) +0.5Gd(cn)). sn: PAAS normalized (McLennan, 1989); cn: chondrite normalized (Taylor and McLennan, 1985).

Appendix B1.

	kenomagnetite-I (itabirite)			lamelar hematite (itabirite)			kenomagnetite-I (HGI)			Martite-I (HGI)			Hematite granoblastic (HGI)		
	ppm (mean)	sd	n	ppm (mean)	sd	n	ppm (mean)	sd	n	ppm (mean)	sd	n	ppm (mean)	sd	n
Mg	2.54	0.681	9	2.47	0.34	2	697	322	21	58	96	31	1.99	1.07	26
Al	1171	30.02	18	1139	4.23	4	743	148	21	1119	154	31	819	473	26
P	<LOD		0	<LOD		0	9.58	0	1	73	33	31	18	15	4
Ti	95.49	8.50	18	93	5.03	4	11	18	21	1.45	1.34	17	81	46	26
V	33.35	0.65	18	33	0.48	4	55	20	21	11	9.94	31	39	3.62	26
Cr	6.24	2.33	18	3.84	0.33	4	15	3.3	21	5.95	5.26	31	29	36	26
Mn	3.24	0.57	5	3.34	0.61	3	815	568	21	433	831	31	9	4.40	26
Co	0.04	0.002	2	0.04	0.001	2	2.4	0.46	21	0.71	0.97	31	0.02	0.004	12
Ni	0.19	0.31	4	0.20	0	1	5.44	1.56	21	1.77	2.67	31	0.08	0.01	6
Zn	<LOD		0	<LOD		0	9.92	14	17	3.56	6.7	31	0.15	0.05	6
Ga	0.38	0.084	18	0.35	0.15	4	1.5	1.32	21	1.44	1.34	31	0.57	0.3	26
As	0.43	0.12	12	0.34	0	1	0.3	0.05	5	35	14	31	0.51	0.16	22
Mo	1.73	0.155	18	1.66	0.13	4	0.25	0.12	20	0.35	0.07	31	3.69	1.15	26
Ce	0.016	0	1	<LOD		0	0.01	0.006	3	1.08	1.07	31	0.07	0.09	8

Appendix B1 (cont).

	Hematite tabular (HGI)			Hematite Specular (shear vein)			Martite-II (Vp2 veins)		
	ppm (mean)	sd	n	ppm (mean)	sd	n	ppm (mean)	sd	n
Mg	1.81	0.49	18	0.61	0.24	12	625	46	15
Al	1489	76	18	399	142	13	861	43	15
P	<LOD		0	<LOD		0	156	29	15
Ti	46	22	18	<LOD		0	5.14	1.29	15
V	78	7	18	6	3.75	13	40	1.37	15
Cr	15	6	18	0.75	0.2	6	10	2.83	15
Mn	3.98	0.83	18	1.17	0.29	2	1004	17	15
Co	0.02	0	1	<LOD		0	0.83	0.09	15
Ni	<LOD		0	<LOD		0	1.08	0.18	15
Zn	0.15	0.044	8	0.13	0.01	3	3.33	1.66	15
Ga	1.82	0.15	18	0.58	0.16	13	0.81	0.11	15
As	0.72	0.48	18	0.57	0.42	9	0.65	0.19	14
Mo	15	1.04	18	0.36	0.31	8	0.83	0.19	15
Ce	0.03	0.022	2	<LOD		0	2.21	0.49	15

Appendix B2.

	Martite-I (itabirite)			Lamelar Hematite (itabirite)			kenomagnetite-I (HGI)			Hematite tabular (HGI)			kenomagnetite-I (compact HGI)		
	ppm (mean)	sd	n	ppm (mean)	sd	n	ppm (mean)	sd	n	ppm (mean)	sd	n	ppm (mean)	sd	n
Mg	56	21	18	1.61	0.68	25	26	2.06	4	21	23	17	24679	735	9
Al	845	295	18	776	79	25	66	25	4	3694	1294	17	1359	276	9
P	564	93	18	12	0	1	37	0	1	14	0	1	<LOD		0
Ti	3.91	0	1	142	78	25	1.21	0.33	4	1967	2979	17	117	3	9
V	33	9.21	18	29	6.51	25	94	1	4	99	34	17	75	0.68	9
Cr	6.72	1.99	18	14	8.56	25	3.5	0.53	4	17	15	17	9	2.76	9
Mn	17831	7588	18	37	13	25	1106	20	4	11	9	17	3627	68	9
Co	31	18	18	0.07	0.11	17	4.4	0.08	4	0.06	0.03	12	5	0.11	9
Ni	164	154	18	0.45	0.77	17	11	0.45	4	0.23	0.12	6	7	0.2	9
Zn	129	75	18	0.28	0.22	18	129	6	4	0.86	0.66	8	7	1.95	9
Ga	4.83	1.78	18	0.98	0.18	25	3.44	0.1	4	4.26	2.28	17	2.14	0.1	9
As	15	4.13	18	0.50	0.22	14	0.54	0.1	4	0.44	0.1	2	1.3	0.31	3
Mo	1.2	0.63	18	0.60	0.71	25	<LOD		0	1.45	0.39	17	0.09	0.03	9
Ce	3.4	1.2	18	0.04	0.04	2	0.03	0.005	3	<LOD		0	0.13	0.17	2

Appendix B2 (cont).

ME	Hematite Specular (shear veins)		
	ppm (mean)	sd	n
Mg	0.31	0.14	12
Al	696	95	12
P	9	0	1
Ti	42	3.66	12
V	37	2.18	12
Cr	1.4	0.22	12
Mn	15	3.41	12
Co	0.01	0.0007	2
Ni	0.11	0.03	2
Zn	0.13	0.03	6
Ga	0.99	0.1	12
As	0.44	0.15	6
Mo	0.43	0.1	12
Ce	0.01	0	1

Appendix B3.

	kenomagnetite-I (HGI) (GNH)			Martite-I (HGI) (DGN)			Hematite granoblastic (HGI) (GNH)			kenomagnetite-I (compact HGI) (GNH)			Hematite granoblastic (HGI) (DGN)		
	ppm (mean)	sd	n	ppm (mean)	sd	n	ppm (mean)	sd	n	ppm (mean)	sd	n	ppm (mean)	sd	n
Mg	38545	771	32	908	122	20	402	136	29	25231	791	31	8.23	2.5	36
Al	1838	894	32	3750	814	20	4013	610	29	1425	566	31	6513	292	36
P	16	0	1	1106	693	20	9.08	0	1	<LOD		0	57	64	2
Ti	19	4.52	32	2987	266	20	2635	893	29	108	12	31	323	19	36
V	56	0.93	32	344	16	20	112	27	29	73	1.21	31	94	2.5	36
Cr	32	5	32	226	231	20	21	6.9	29	5.5	1.16	31	99	34	36
Mn	4215	121	32	3863	219	20	30	6.1	29	3637	91	31	9.43	3.2	36
Co	29	0.7	32	7.67	0.39	20	0.18	0.06	28	5.14	0.12	31	0.04	0.01	26
Ni	68	1.73	32	38	1.77	20	0.25	0.08	29	7	0.30	31	0.15	0.04	21
Zn	8	5.88	32	29	20	20	0.24	0.07	20	8	5	31	0.25	0.25	13
Ga	7	0.86	32	8	1.21	20	1.84	0.26	29	2.15	0.2	31	7.33	0.32	36
As	0.35	0.12	16	2.91	0.95	20	0.44	0.08	11	0.51	0.16	22	0.67	0.21	33
Mo	0.07	0.008	4	9	0.74	20	2.09	1.79	29	0.15	0.07	17	1.83	0.17	36
Ce	0.12	0.19	3	0.49	0.36	20	0.02	0.005	4	0.06	0.1	5	0.02	0	1

- Silica leaching from itabirite led to the formation of high-grade iron orebodies.
- The formation of the high-grade iron orebodies is accompanied by the magnetite oxidation, and the recrystallization of martite to granoblastic hematite.
- Recrystallization of hematite is accompanied by enrichment in immobile elements (Ti, Al, V, Cr and Mo) due to removing of mobile elements (Mg, Mn, and As).
- Iron enrichment in the high-grade orebodies is related to the influx of anatectic fluids.

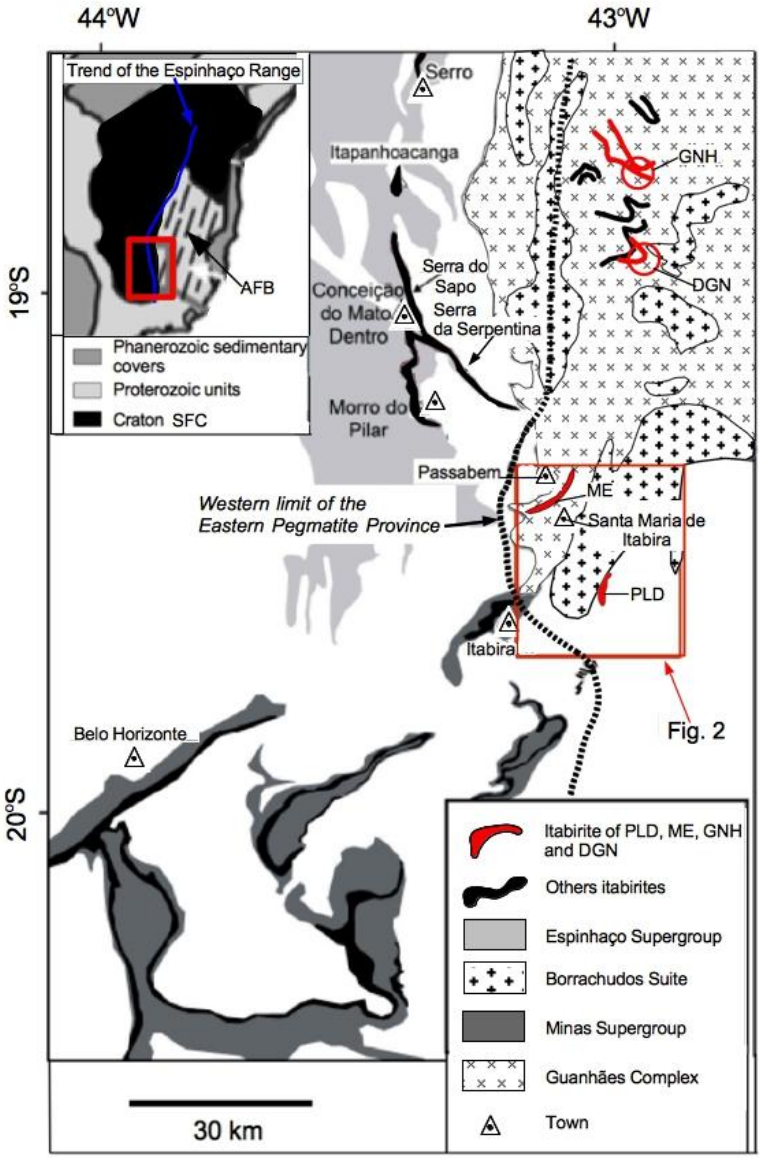

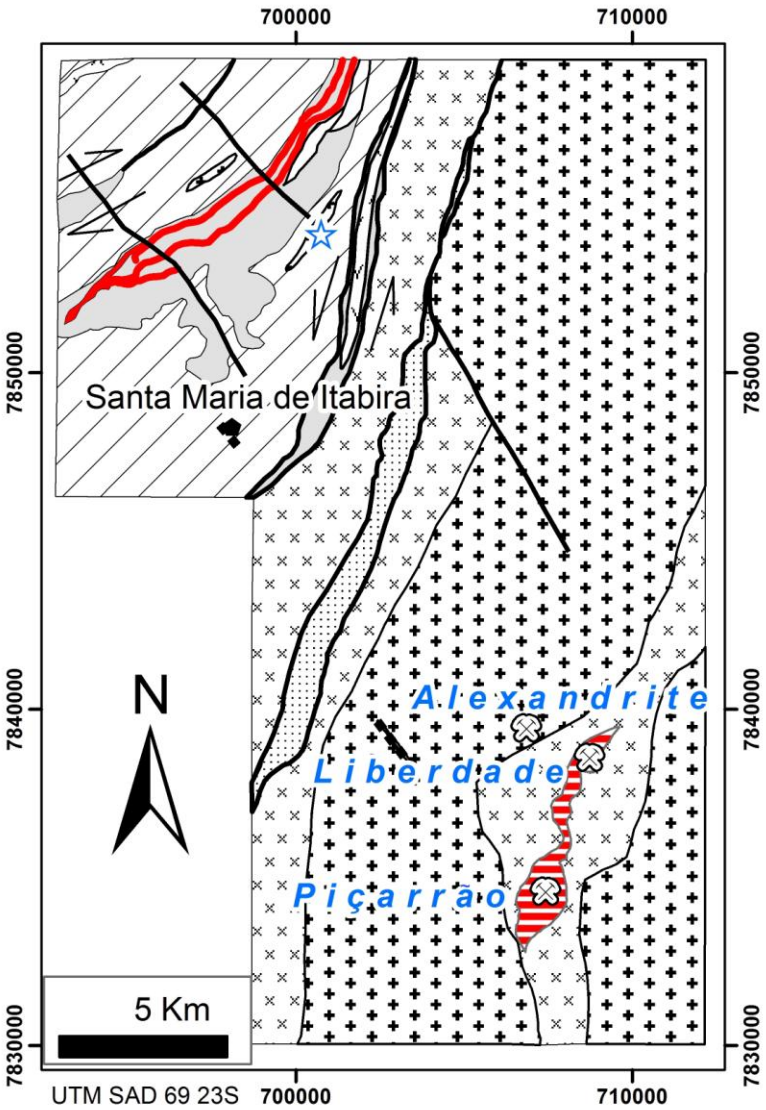

Dikes

Pedro Lessa Suite

Amphibolite

Morro Escuro Sequence

Quartz schist and quartzite

Itabirite

Borrachudos Suite

Açucena Granite

Serra da Pedra Branca Unit

Quartzite

Guanhães Complex

Banded gneiss and quartz schist

Itabirite

Archean Basal Complex

Orthogneiss

Structural lineament

Shear zone

Mine

Artisanal beryl mining area
Ponte da Raiz Pegmatite

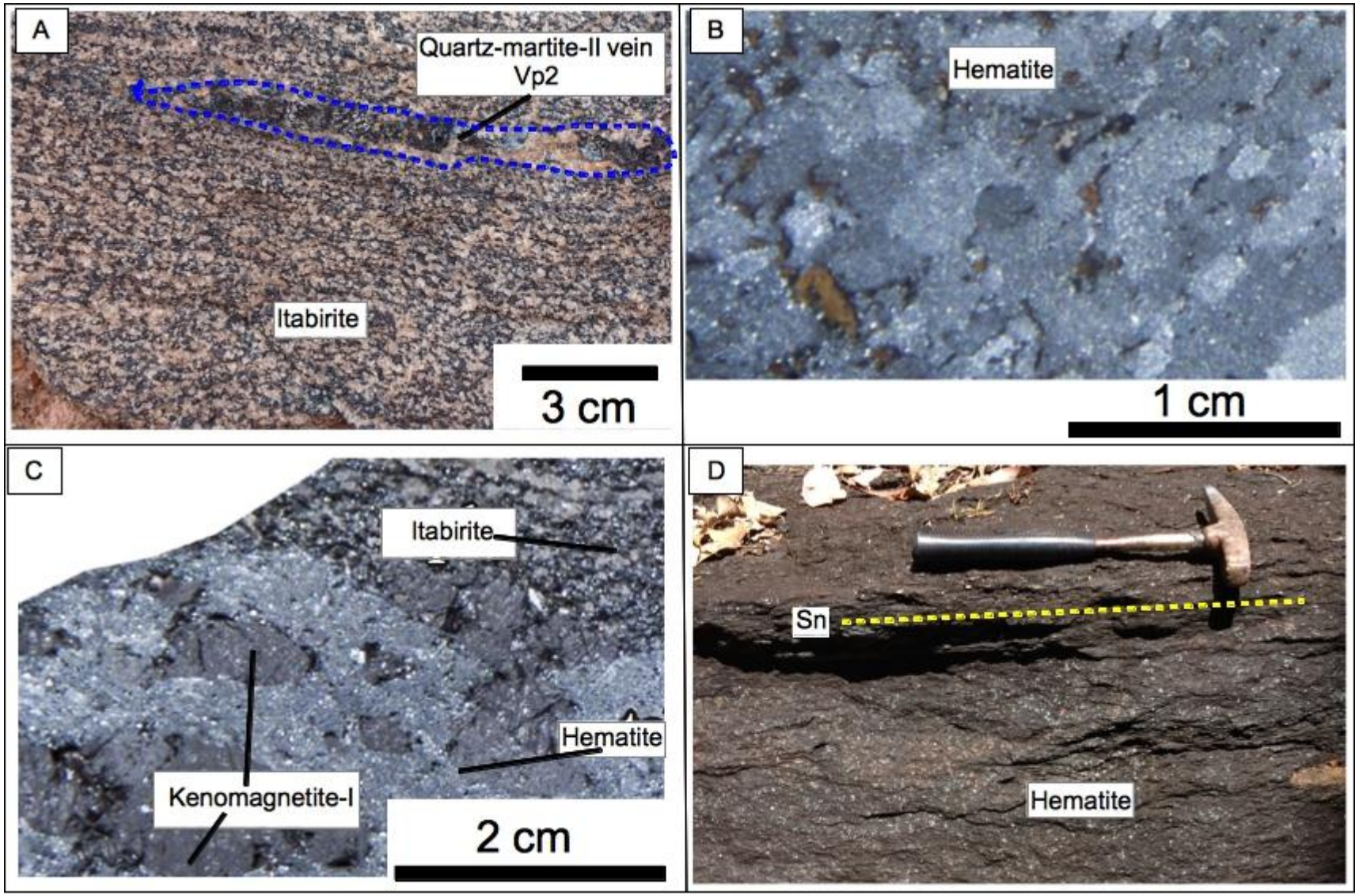

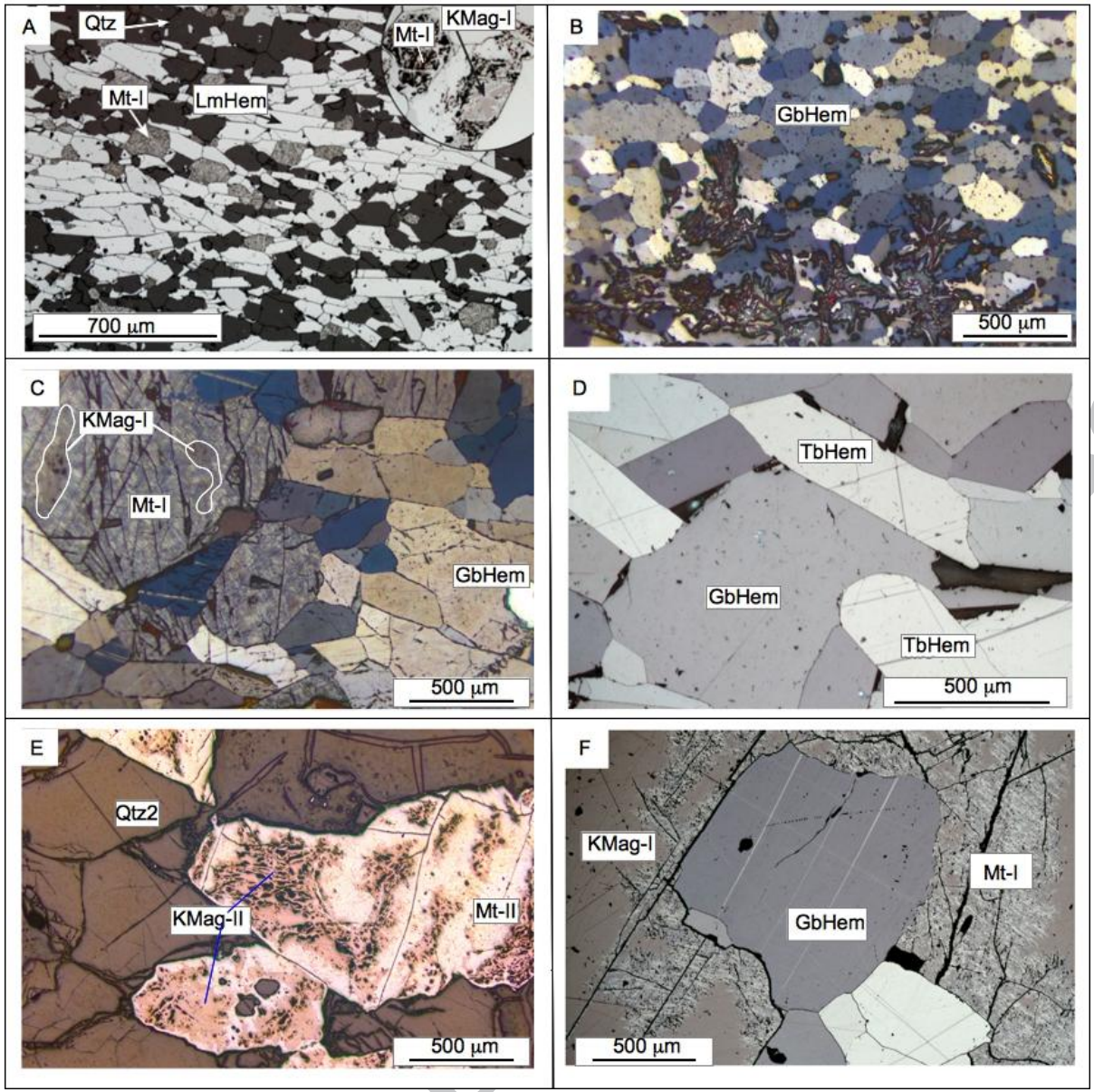

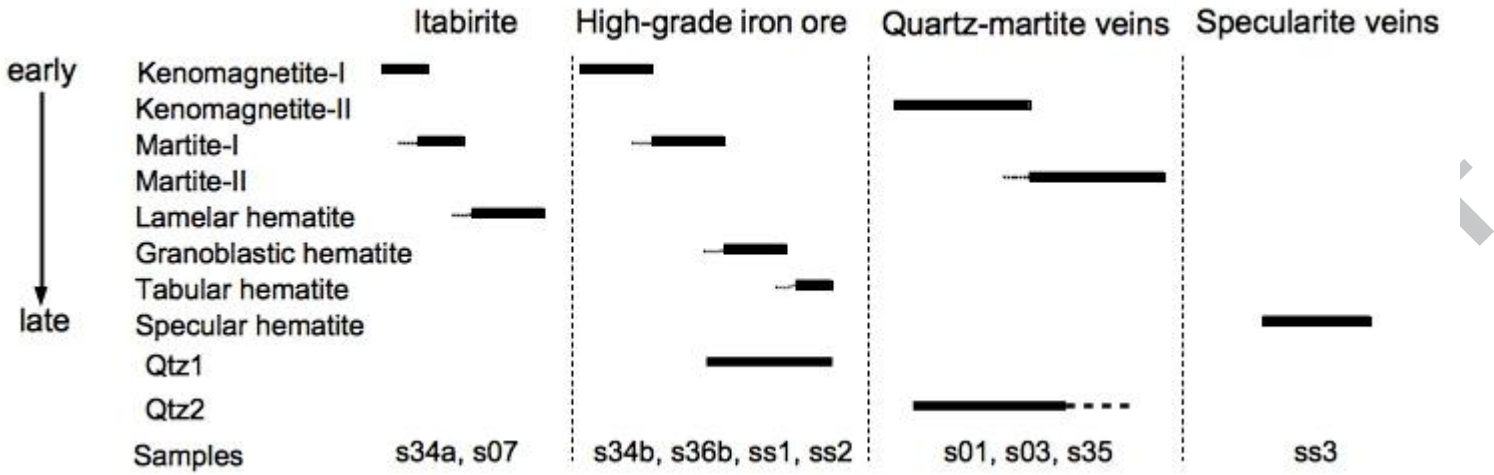

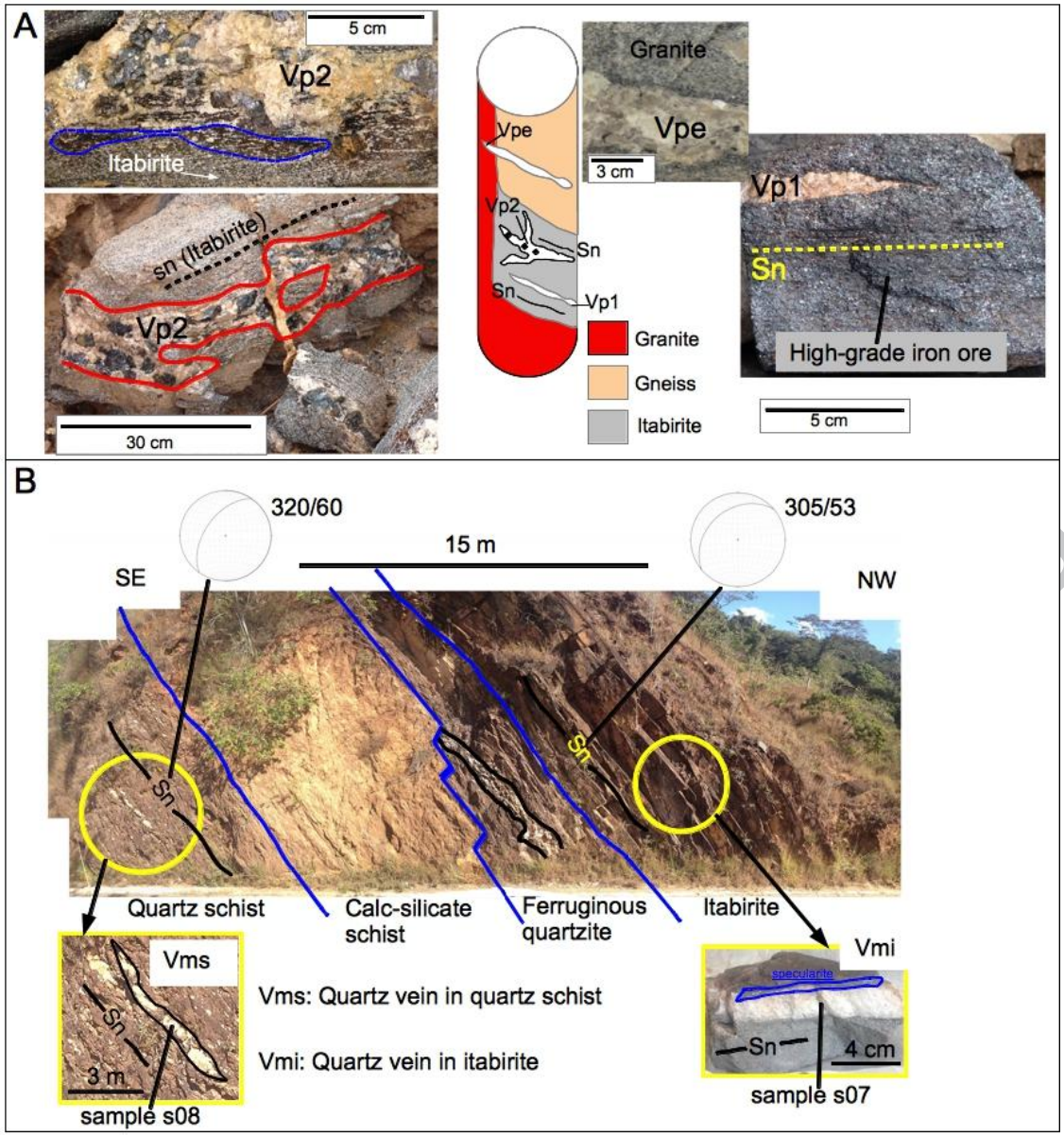

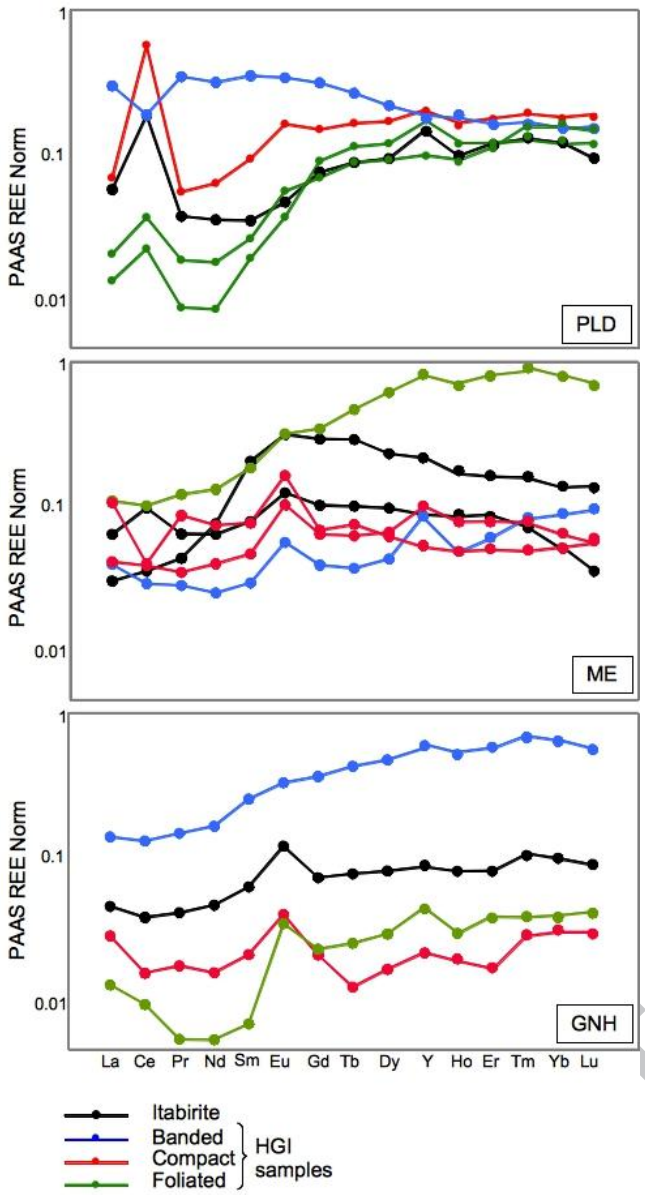

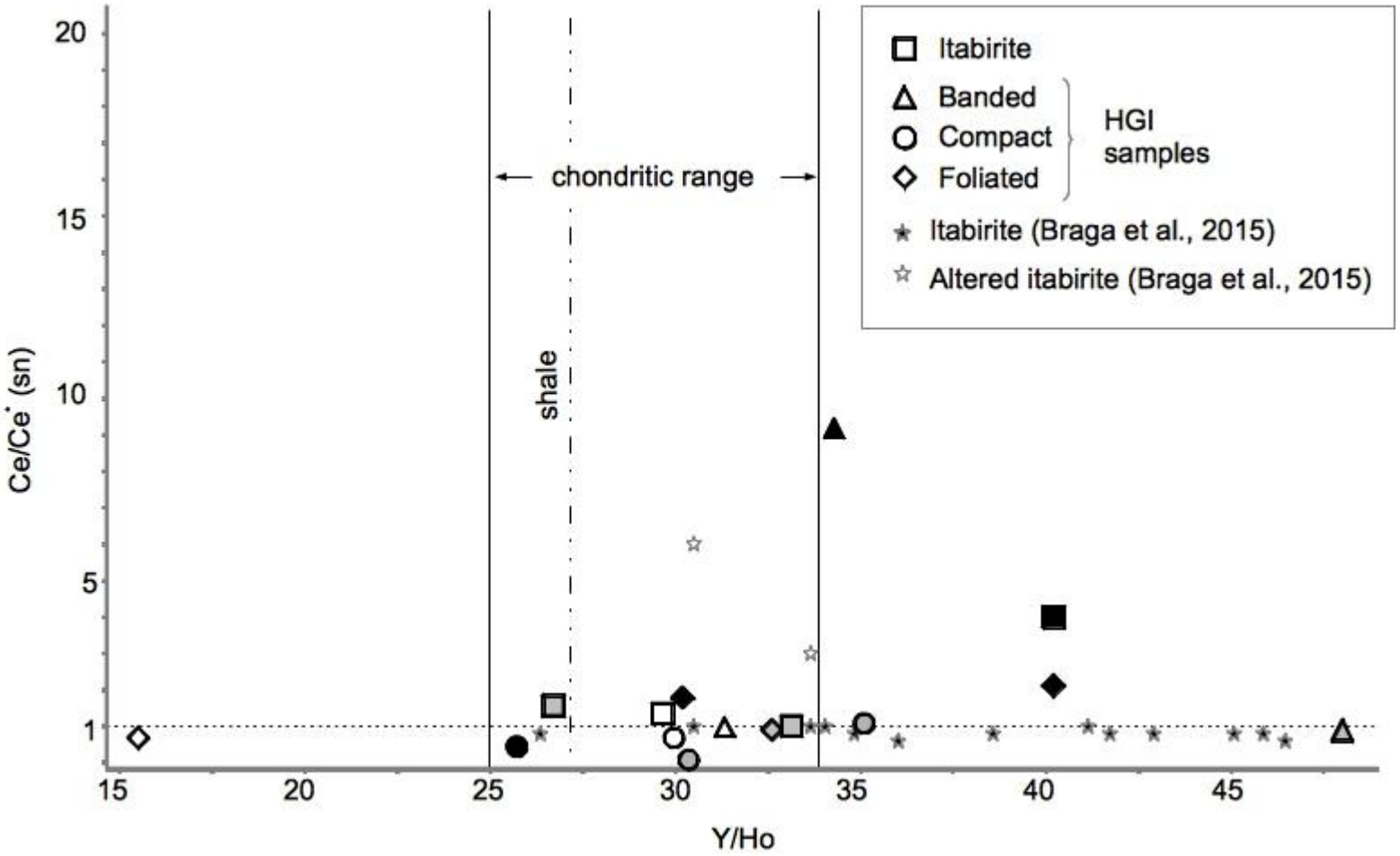

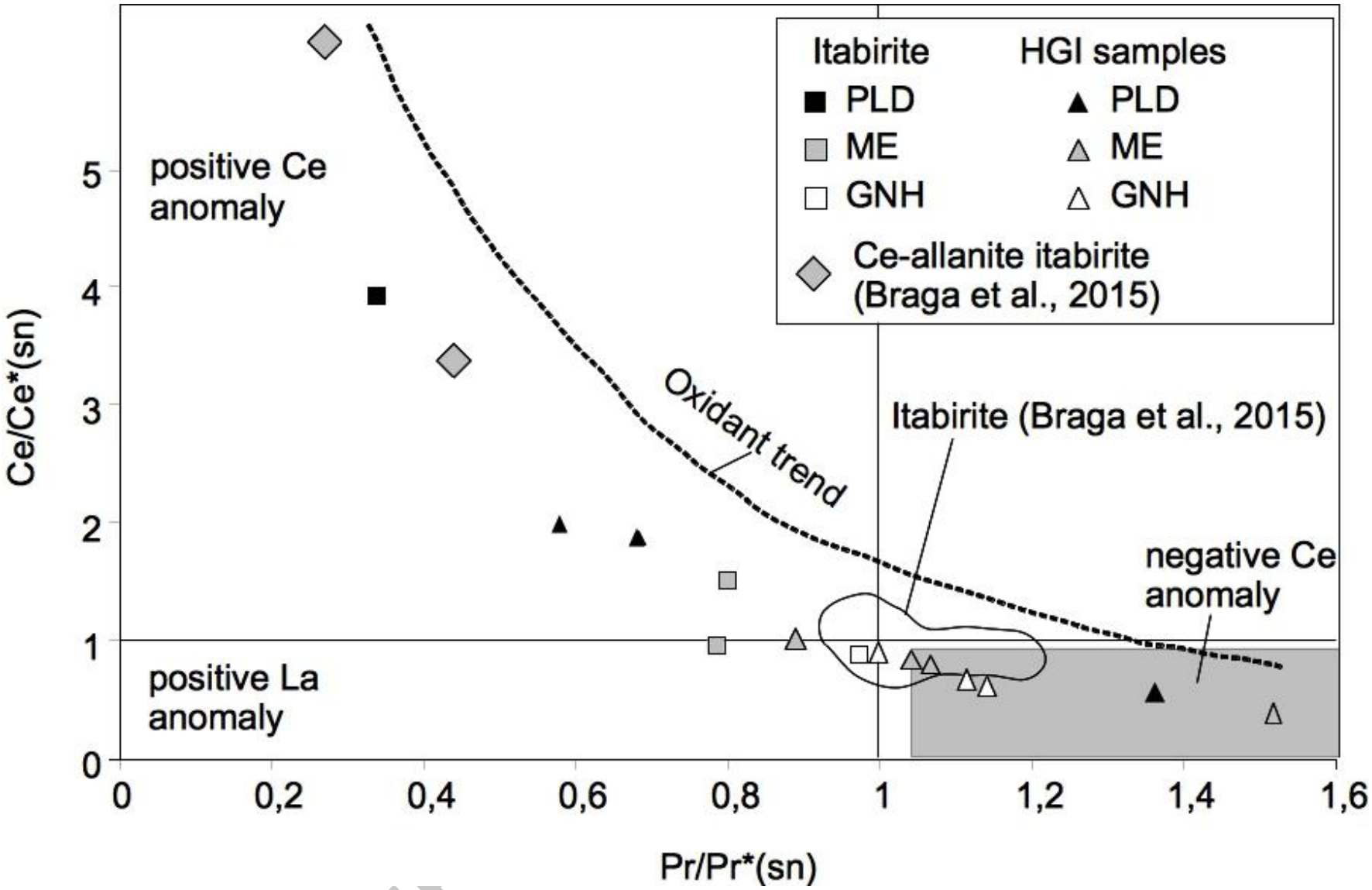
Itabirite
PLD
ME
GNH
HGI samples
PLD
ME
GNH
Ce-allanite itabirite
(Braga et al., 2015)
positive Ce
anomaly
Oxidant trend
Itabirite (Braga et al., 2015)
negative Ce
anomaly
positive La
anomaly
Ce/Ce*(sn)
Pr/Pr*(sn)
0
1
2
3
4
5
0
0,2
0,4
0,6
0,8
1
1,2
1,4
1,6

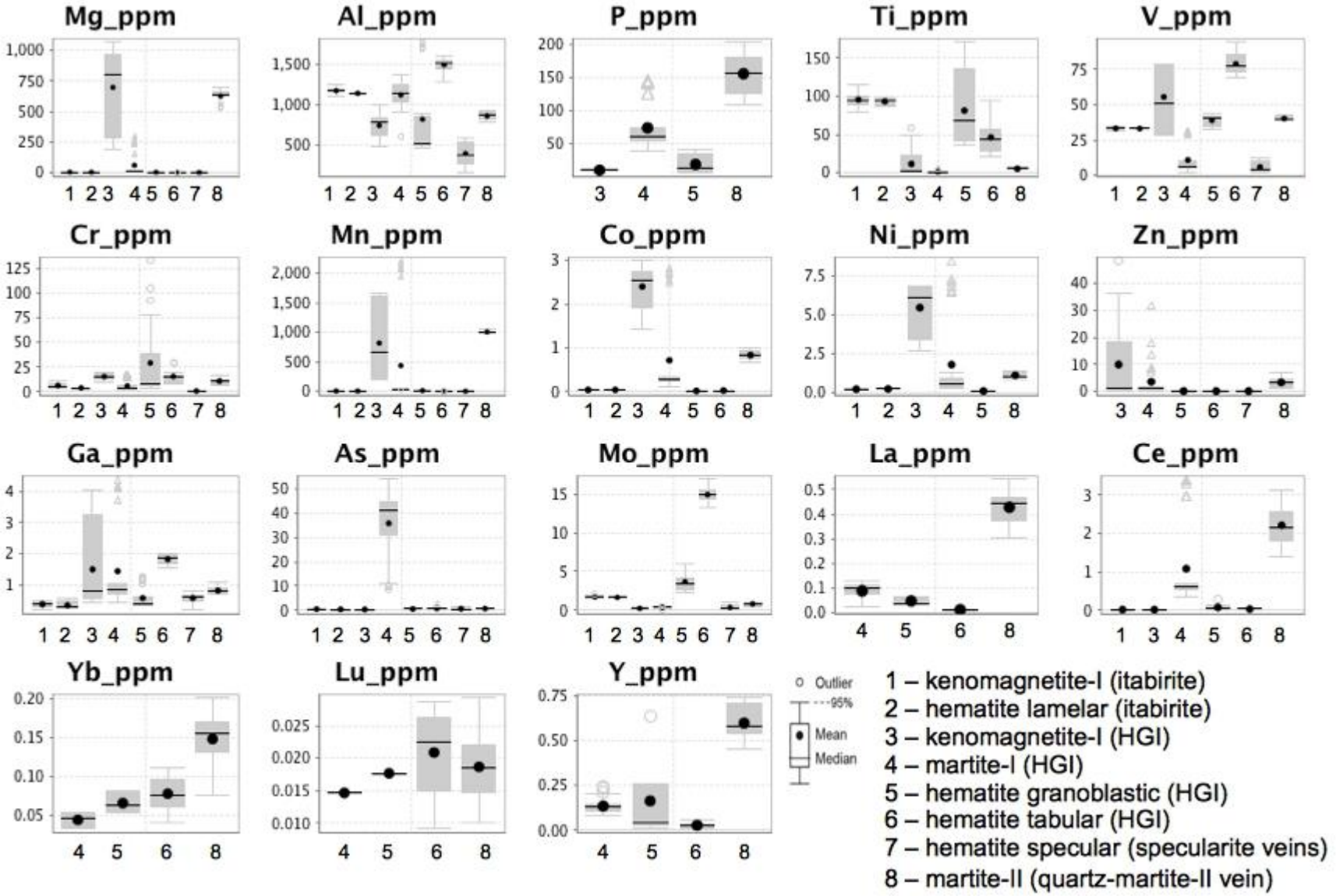

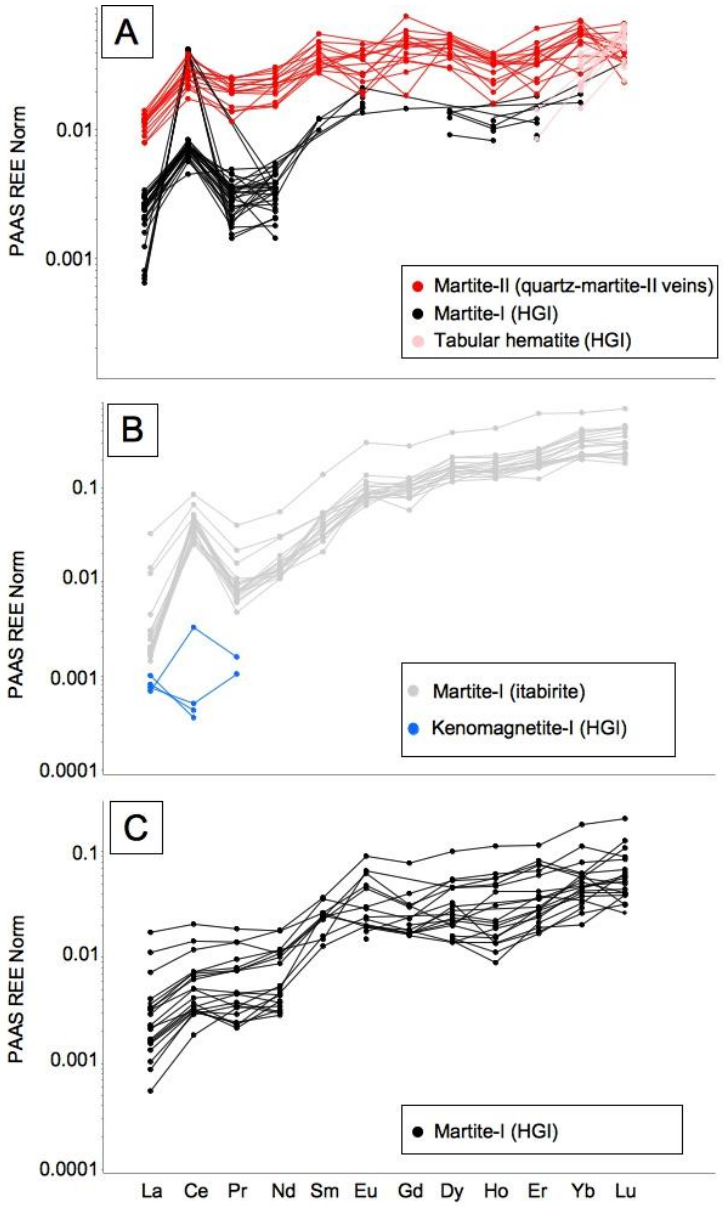

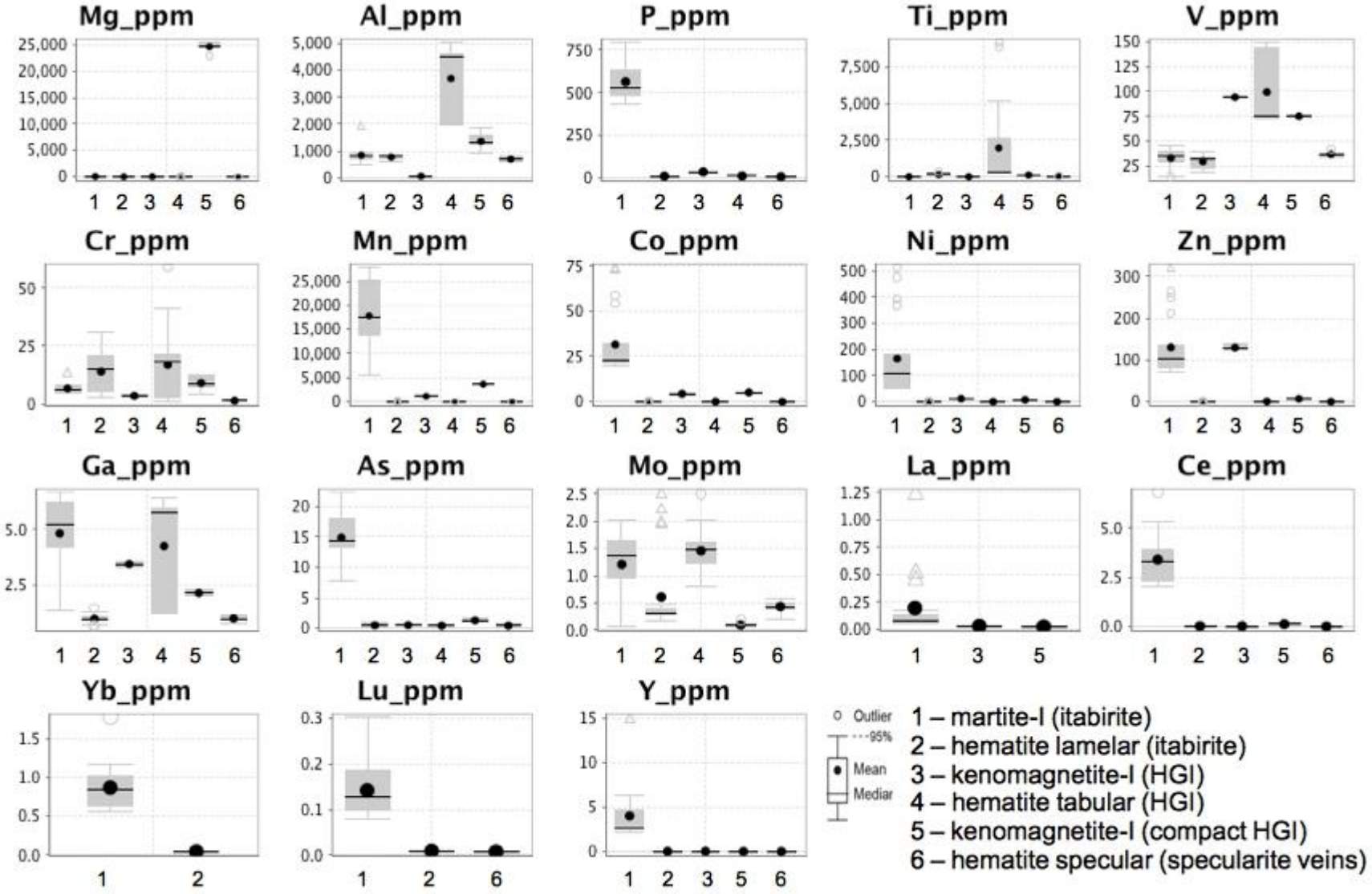

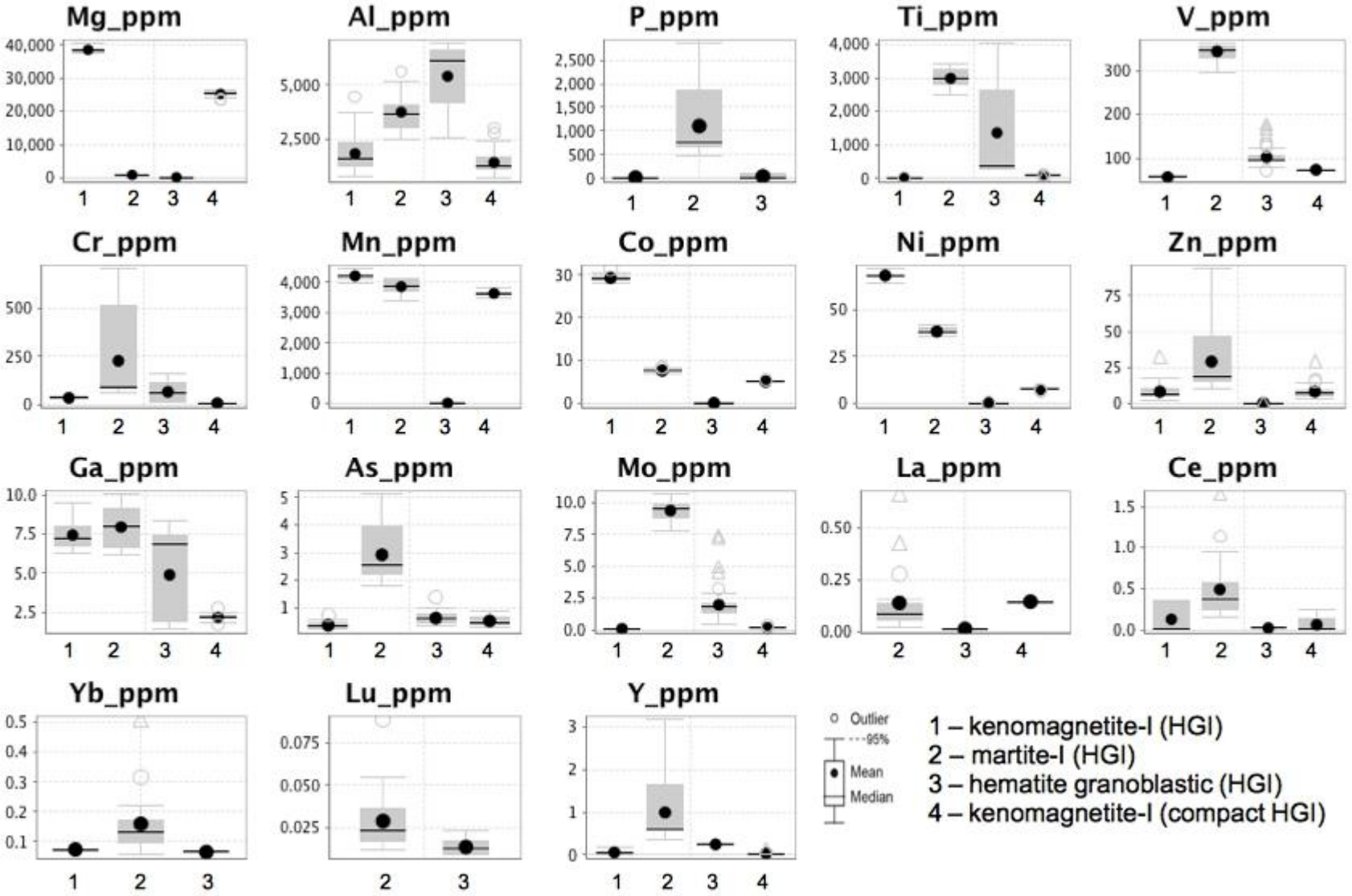

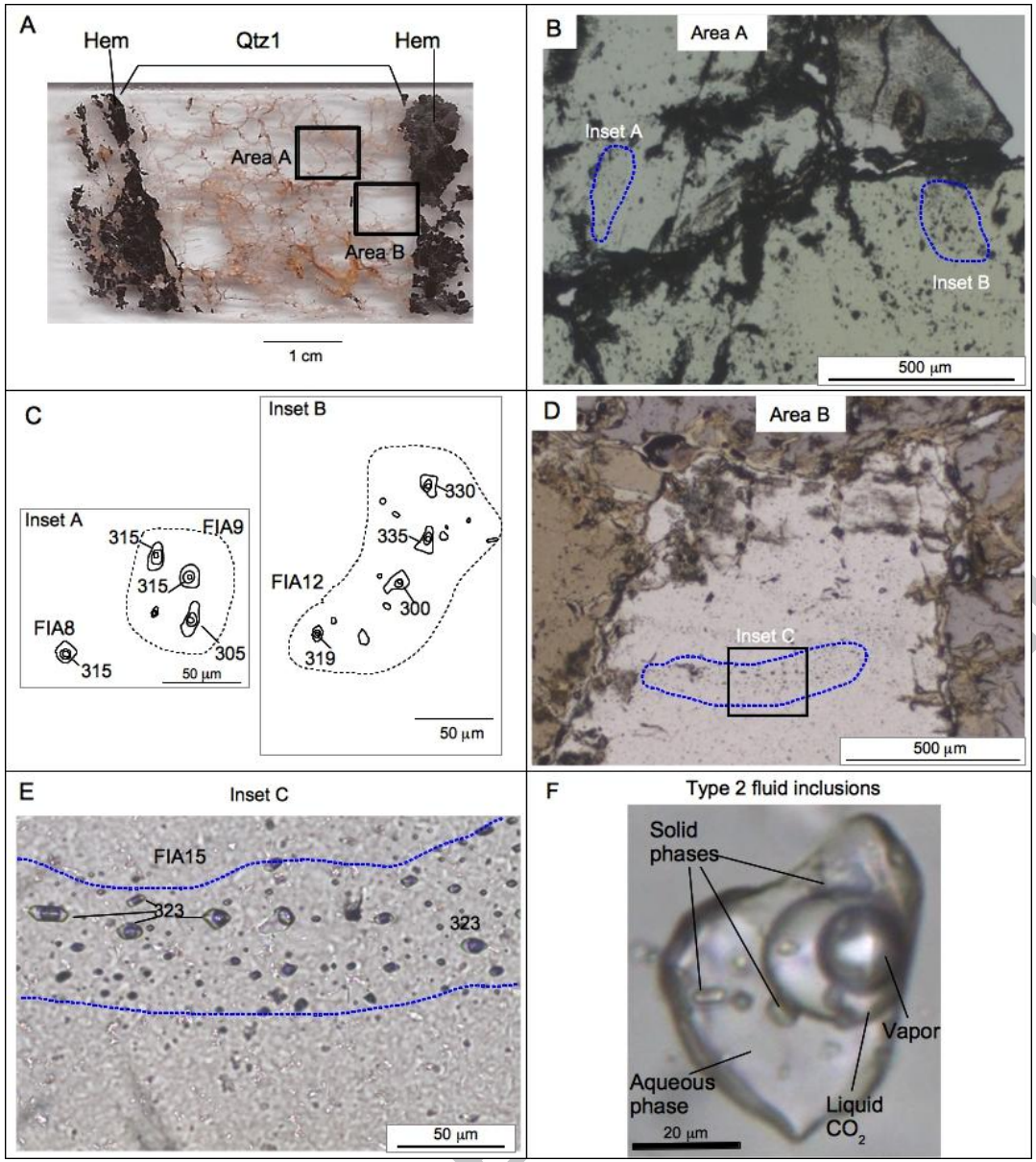

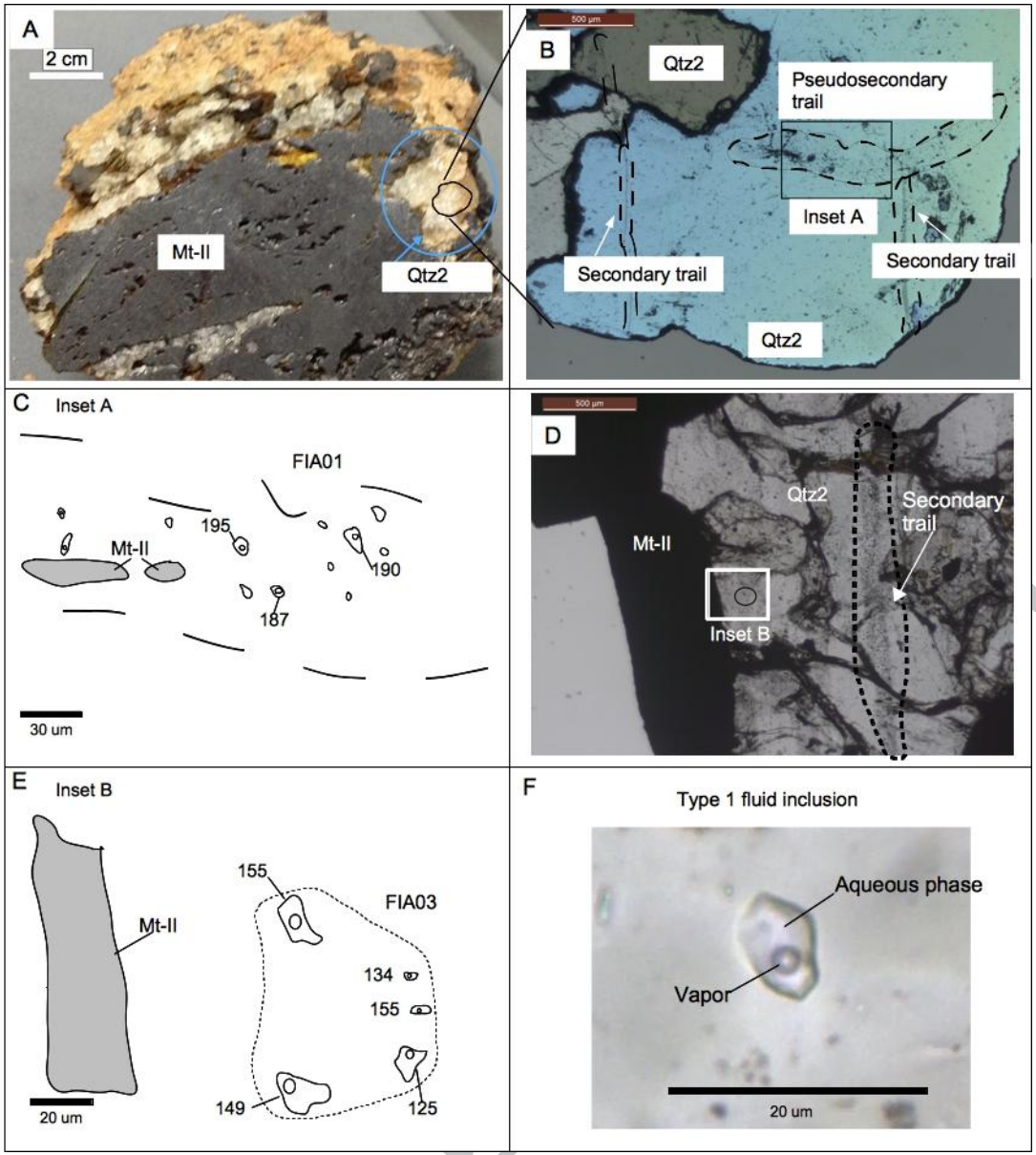

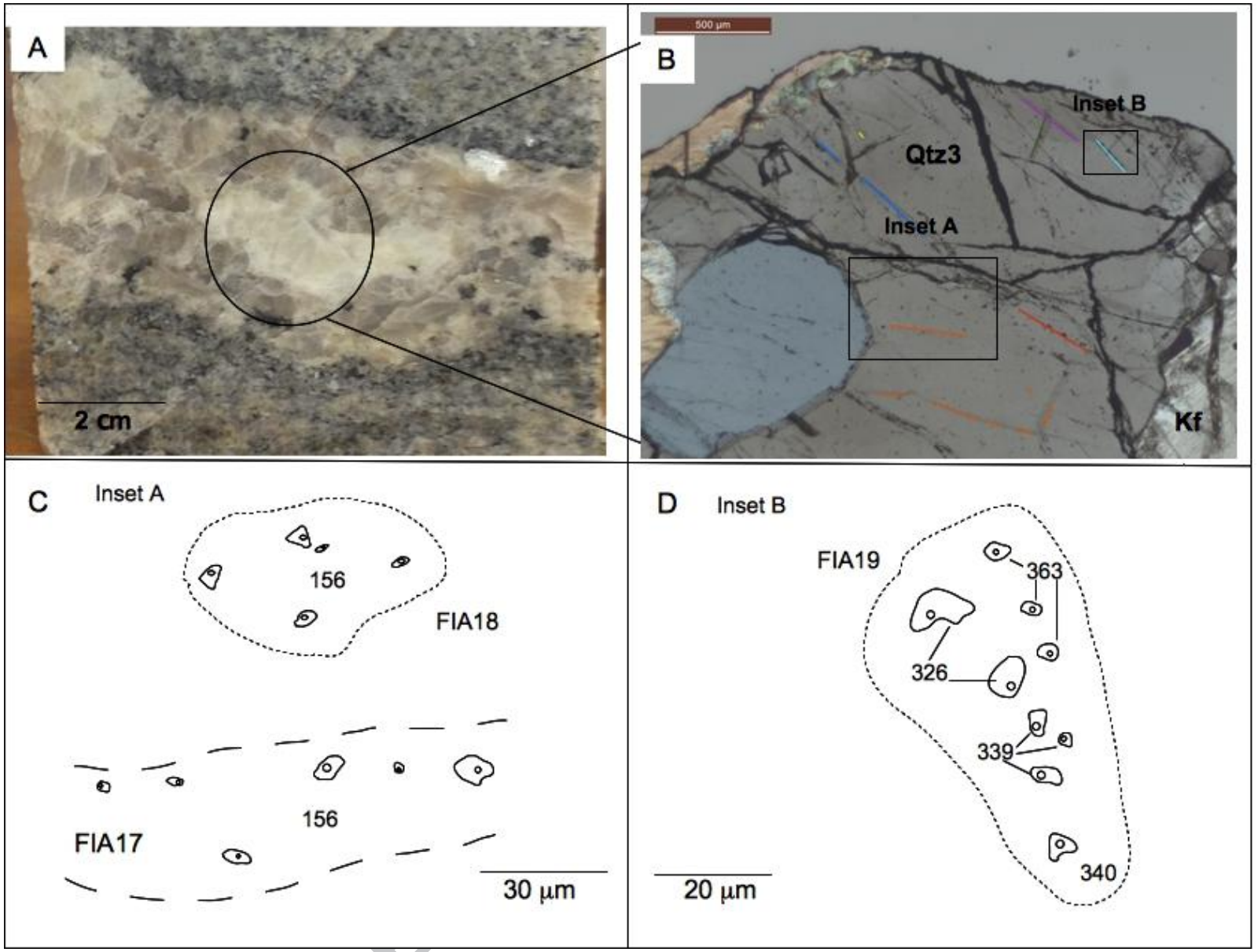

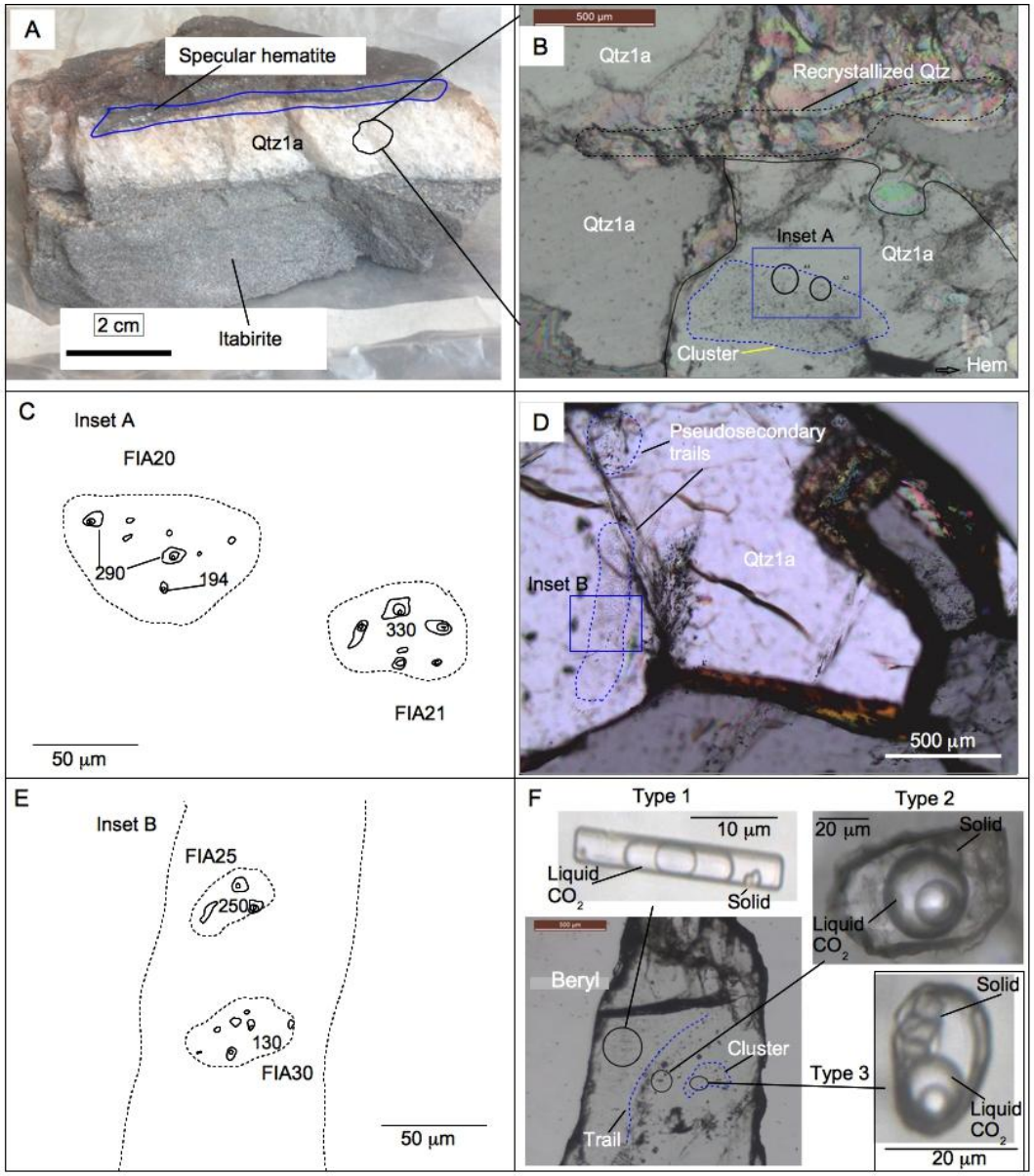

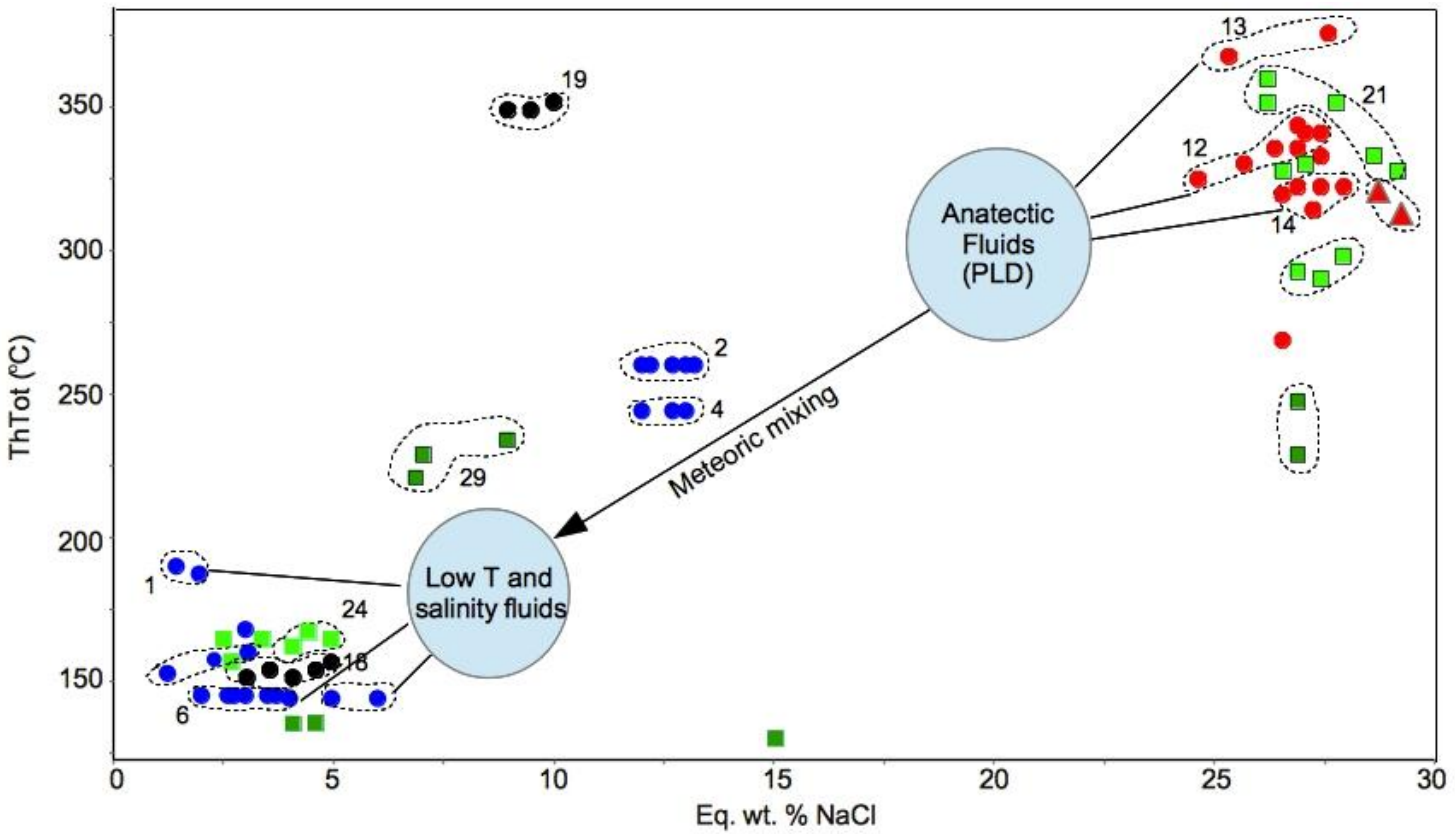

Vein type	Aqueous	Aqueous-carbonic
Vp1		●
Vp2	●	
Vpe	●	
Vmi	■	■
Vms	■	■
Vb		▲

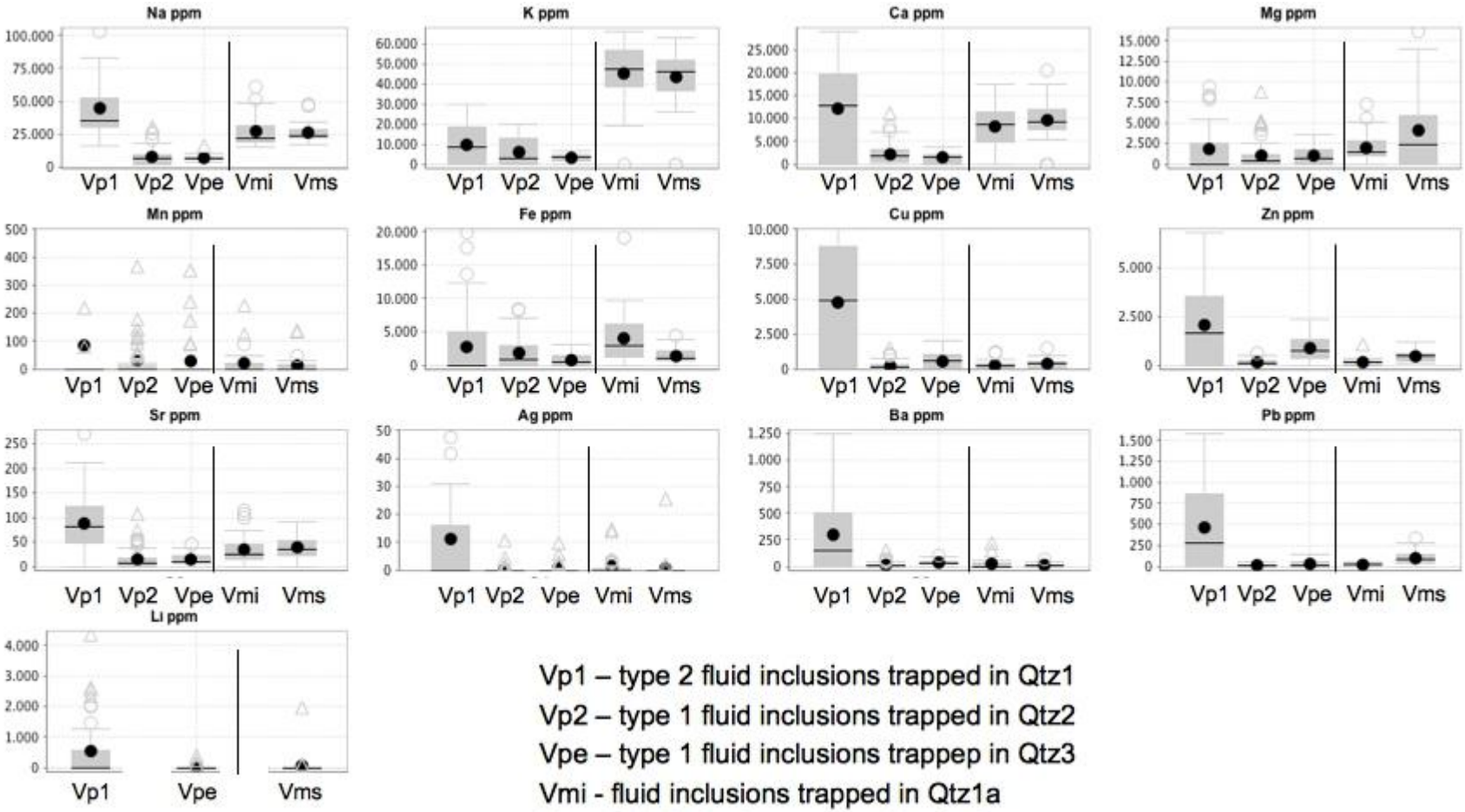

Vp1 – type 2 fluid inclusions trapped in Qtz1
Vp2 – type 1 fluid inclusions trapped in Qtz2
Vpe – type 1 fluid inclusions trappep in Qtz3
Vmi - fluid inclusions trapped in Qtz1a
Vms -fluid inclusions trapped in Qtz1a

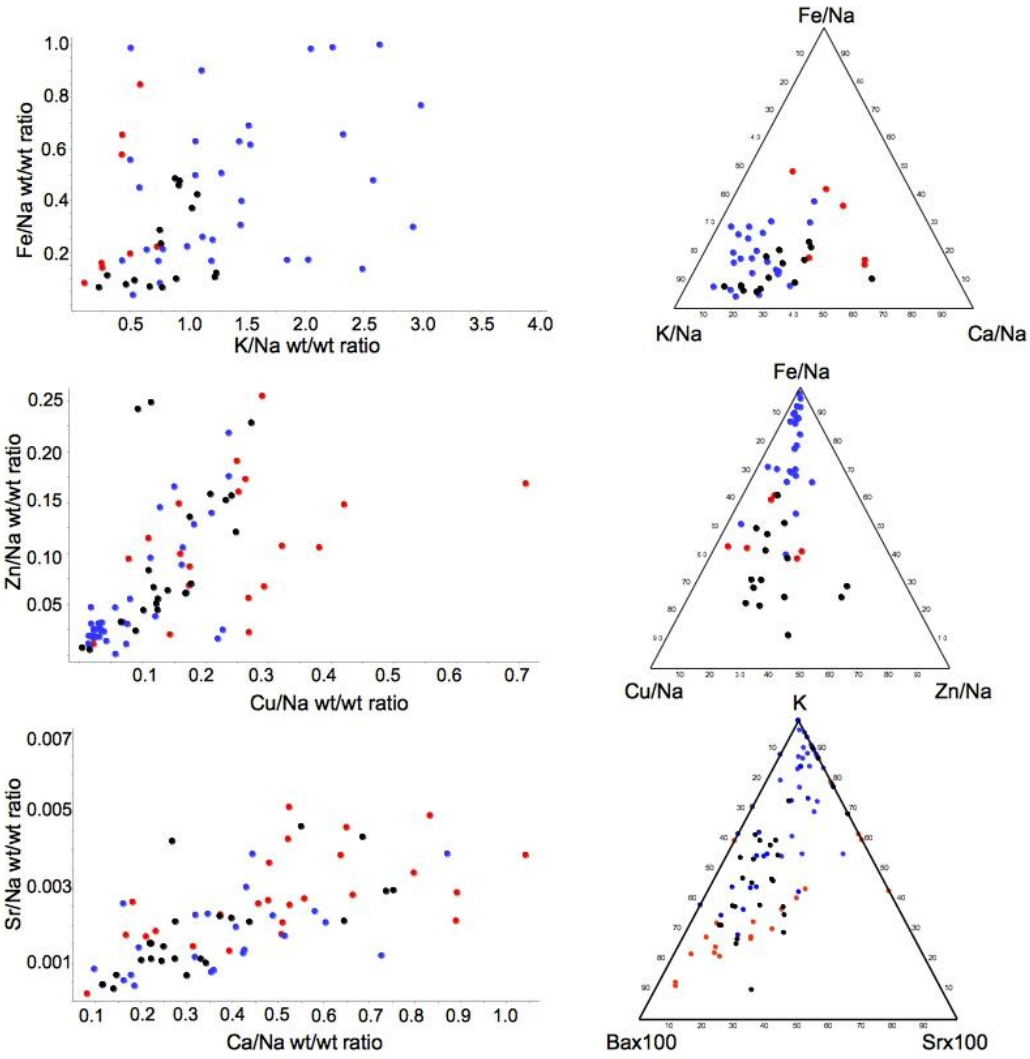

- type 2 fluid inclusions trapped in Qtz1 – quartz Vp1 veins hosted in HGI
- type 1 fluid inclusions trapped in Qtz2 – quartz-martite-II Vp2 veins
- type 1 fluid inclusions trappep in Qtz3 – quartz-K-feldspar-plagioclase Vpe veins

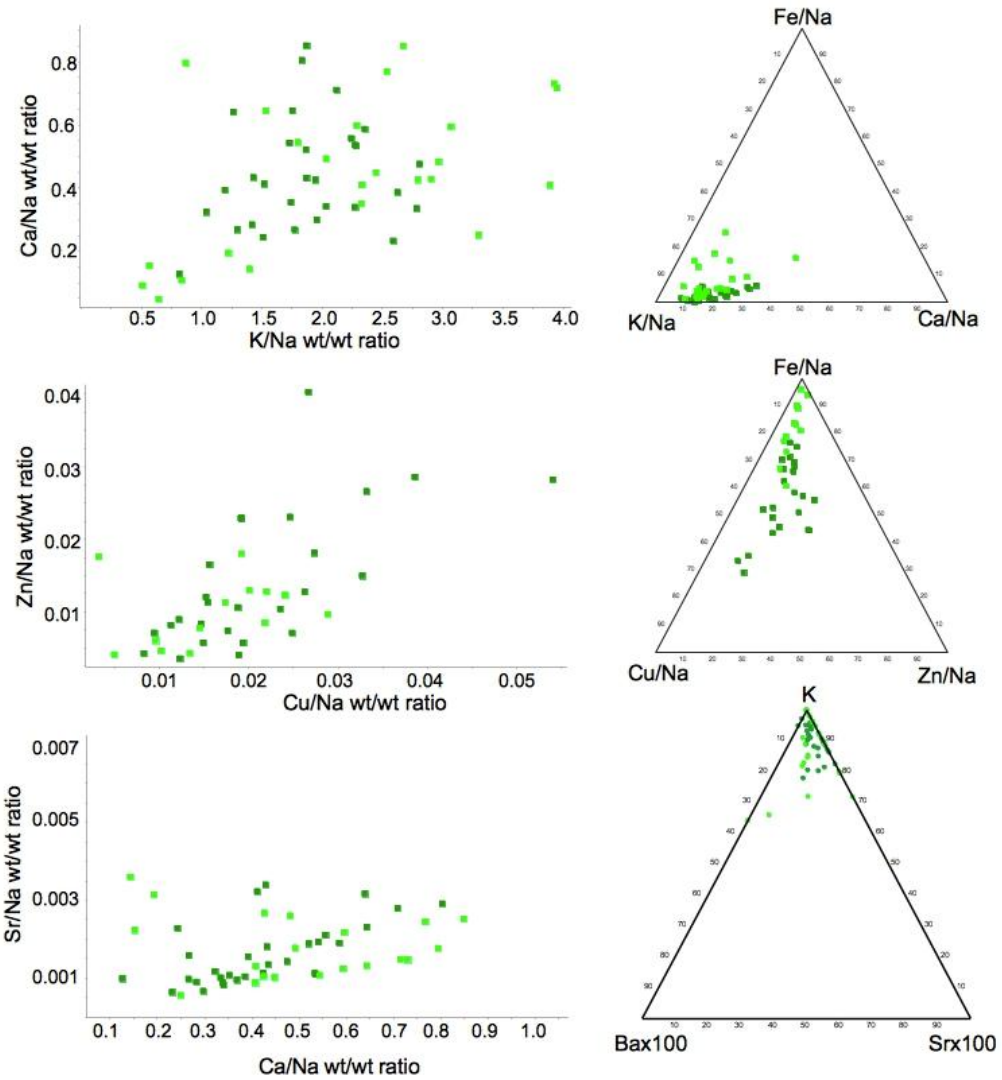

fluid inclusions trapped in Qtz1 – quartz Vmi veins hosted in itabirite

fluid inclusions trapped in Qtz1 – quartz Vms veins hosted in quartz schist